Journal of Nanobiotechnology

RESEARCH

Open Access

Inhalable biomimetic polyunsaturated fatty acid-based nanoreactors for peroxynitrite-augmented ferroptosis potentiate radiotherapy in lung cancer

Yiting Chen[1†], Xueli Huang[1†], Ruining Hu[1], Enhao Lu[1], Kuankuan Luo[1], Xin Yan[1], Zhiwen Zhang[1], Yan Ma[4*], Minghe Zhang[3*] and Xianyi Sha[1,2*]

Abstract

The limited efficacy and poor tumor accumulation remain crucial challenges for radiotherapy against lung cancer. To address these limitations, we rationally developed a polyunsaturated fatty acid (PUFA)-based nanoreactor (DHA-N@M) camouflaged with macrophage cell membrane to improve tumoral distribution and achieve peroxynitrite-augment ferroptosis for enhanced radiotherapy against lung cancer. After nebulization, the nanoreactors exhibited superior pulmonary accumulation in orthotopic lung cancer-bearing mice, with 70-fold higher than intravenously injected nanoreactors at 12 h post-administration, and distributed deeply in the tumors. DHA-N@M selectively released nitric oxide (NO) in glutathione (GSH)-enriched tumor cells, with consumption of GSH and subsequent inactivation of glutathione peroxidase 4 (GPX4). Under radiation, NO reacted with radiotherapy-induced reactive oxygen species (ROS) to generate peroxynitrite ($ONOO^-$), resulting in redox homeostasis disruption. Combined with docosahexaenoic acid (DHA)-induced lipid metabolism disruption, overwhelming ferroptosis was induced both in vitro and in vivo. Notably, DHA-N@M mediated ferroptosis-radiotherapy significantly suppressed tumor growth with a 93.91% inhibition in orthotopic lung cancer models. Therefore, this design provides a nebulized ferroptosis-radiotherapy strategy for lung cancer.

Keywords Radiotherapy, Ferroptosis, Lung cancer, Inhalation, Nanoreactor

†Yiting Chen and Xueli Huang contributed equally to this work.

*Correspondence:
Yan Ma
mayan@smhc.org.cn
Minghe Zhang
minghezhang@smmu.edu.cn
Xianyi Sha
shaxy@fudan.edu.cn

[1]Department of Pharmaceutics, School of Pharmacy, Key Laboratory of Smart Drug Delivery, Fudan University, Ministry of Education, Lane 826, Zhangheng Road, Shanghai 201203, China
[2]Quzhou Fudan Institute, 108 Minjiang Avenue, Kecheng District, Quzhou 324002, Zhejiang Province, China
[3]Naval Medical Center, Naval Medical University, Shanghai, Shanghai 200052, China
[4]Department of Pharmacy, Shanghai Mental Health Center, Shanghai Jiao Tong University School of Medicine, Shanghai 201108, China

Introduction

Lung cancer is the most prevalent malignancy globally and has the highest mortality rate among cancers [1]. Radiotherapy, a favored option for treating inoperable early-stage or locally advanced lung cancer patients [2, 3], could directly damage DNA structure *via* ionizing radiation and induce abundant reactive oxygen species (ROS) to aggravate cellular injury [4]. However, the evasion of apoptosis serving as a characteristic feature of tumors and the high glutathione (GSH) in tumor microenvironment (TME) neutralizing ROS are associated with the inadequate efficacy of radiotherapy, restricting its clinical application [5].

Compelling evidence indicates a close association between radiotherapy and ferroptosis, a regulated form of non-apoptotic cell death characterized by lethal accumulation of lipid peroxides (LPO) [6]. ROS generated during radiotherapy can oxidize biomolecules, particularly polyunsaturated fatty acids (PUFA), resulting in lipid peroxidation and ferroptosis [7]. Nevertheless, tumor cells are well-equipped with an elevated level of GSH ($1\times10^{-3}\sim10\times10^{-3}$ M) [8], which is involved in ROS scavenging and act as a cofactor for glutathione peroxidase 4 (GPX4) to catalyze LPO into non-toxic alcohol forms, hindering the ferroptosis and radiotherapeutic effect [9, 10]. Thus, PUFA supplementation coupled with GSH depletion may potentiate the synergistic effects between ferroptosis and radiotherapy. To this end, S-nitrosothiol (SNO) comes into our sight because of its GSH-triggered nitric oxide (NO) release profile [11, 12]. It not only consumes GSH but also releases NO, reacting with ROS to form an extremely reactive species of peroxynitrite ($ONOO^-$), thus intensifying oxidative stress [13, 14]. In this regard, designing an SNO-grafted PUFA conjugate would offer a new perspective for ferroptosis/radiation synergistic therapy. Herein, we designed DHA-SNO by grafting SNO onto docosahexaenoic acid (DHA), an endogenous PUFA containing three biallylic groups that readily undergo oxidation.

The unreliable delivery efficiency of systemic administration routes, e.g., intravenous (i.v.) or oral, constitutes another critical bottleneck for lung cancer therapy. This challenge can be overcome *via* intratracheal (i.t.) administration of macrophage cell membrane-based nanovesicles. On one hand, i.t. administration optimizes the pulmonary bioavailability of active ingredients [15, 16]. On the other hand, macrophages, overexpressing integrin α4, can interact with overexpressed vascular cell adhesion molecule-1 (VCAM-1) on lung cancer cells and be efficiently recruited to the tumor region by the chemokine C-C motif ligand 2 (CCL2), making macrophage membrane-based nanovesicles excellent carriers for enhanced delivery to lung tumors [17–20].

In this work, we firstly developed an inhalable biomimetic nanoreactor (termed as DHA-N@M) by inserting DHA-SNO into macrophage cell membrane nanovesicle, with favorable retention in lung tumors to potentiate the ferroptosis-radiotherapy (Fig. 1). Through i.t.

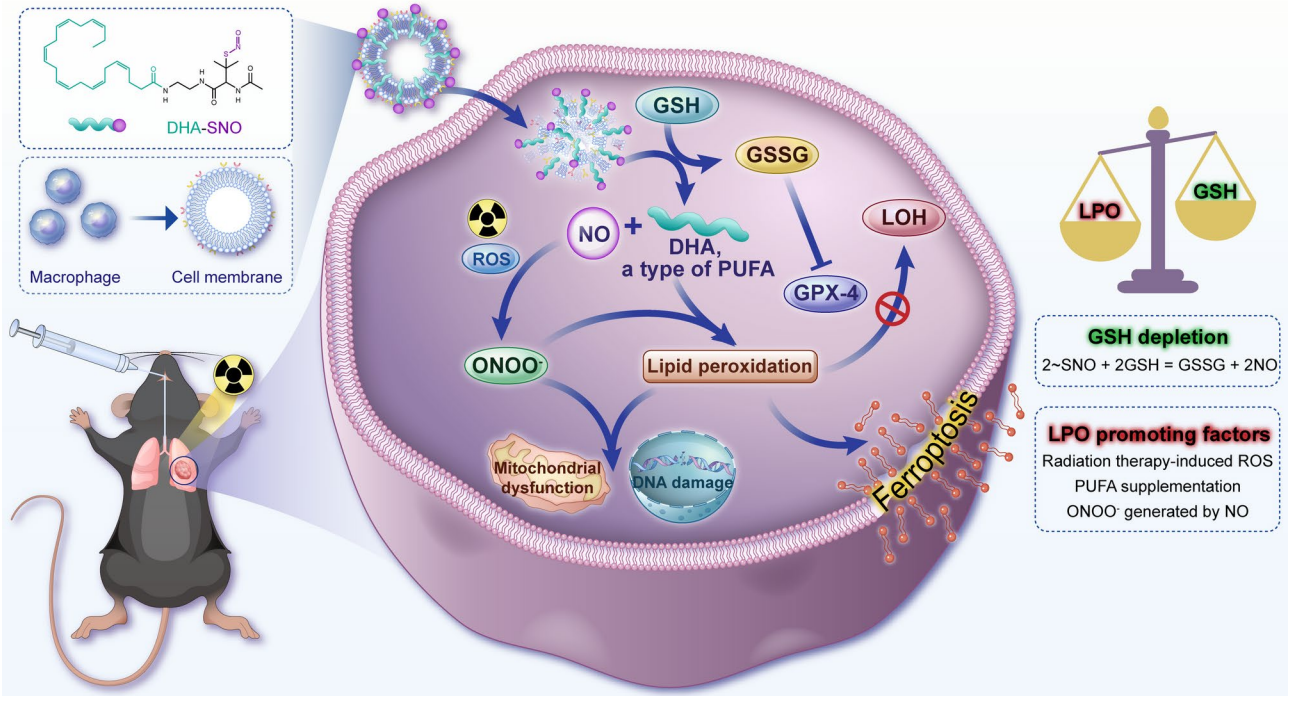

Fig. 1 Schematic illustration of the preparation of DHA-N@M, and the mechanism of radiotherapy-enhanced ferroptosis (Created by FigDraw)

administration and macrophage membrane assistance, DHA-N@M could accumulate in lung tumors and be uptaken by lung cancer cells. Upon internalization, NO was expected to be released in the GSH-enriched tumor cells, along with GSH depletion and subsequent GPX4 inactivation. Then, radiotherapy-generated ROS would react with NO forming highly toxic $ONOO^-$. Simultaneously, DHA underwent chain oxidation to form LPO in the context of high ROS/$ONOO^-$ and impaired GSH/GPX4, ultimately inducing perturbation of lipid metabolism homeostasis, mitochondrial disfunction, DNA damage, and ferroptotic cell death. Therefore, this inhalable nanoreactor with robust redox and lipid metabolism homeostasis disruption ability provides a promising paradigm for ferroptosis-radiotherapy in lung cancer treatment.

Materials and methods

Materials

Anti 3-nitrotyrosine (3-NT), anti-GPX4, anti-integrin α4, anti-γ-H2AX, and DAR-1 were provided by Abcam (Cambridge, UK). The organic solvents used in synthesis procedure were obtained from Adamas (Shanghai, China). 5,5'-Dithiobis-2-nitrobenzoic acid (DTNB), N-Boc-ethylenediamine, and N, N-diisopropylethylamine (DIPEA) were came from Aladdin Biochemical Technology Co., Ltd (Shanghai, China) and the other chemicals for synthesis were brought from Bidepharm (Shanghai, China). Ferrostain-1 (Fer-1), Necrostatin-1 (Nec-1), and Z-VAD-Fmk were provided by Bidepharm (Shanghai, China). Cell counting kit-8 (CCK-8) assay kit, Bicinchoninic acid (BCA) assay kit, D-luciferin potassium salt, 1'-dioctadecyl-3,3,3',3'-tetramethylindodicarbocyanine,4-chlorobenzenesulfonate salt (DID), 2-(4-amidinophenyl)-6-indolecarbamidine (DAPI), DAF-FM, and Evans Blue were obtained from Dalian Meilun Biotechnology Co., Ltd (Dalian, China). Cell lysis buffer, phenylmethanesulfonylfluoride (PMSF), GSH, membrane and cytosol protein extraction kit, chemokine C-C motif receptor 2 (CCR2) antibody, 2,7-dichlorofluorescin diacetate (DCFH-DA), anti-β-actin, and Triton X-100 (10%) were bought from Beyotime Biotechnology Co., Ltd (Shanghai, China). GelNest™ was from NEST Biotechnology (Wuxi, China). Egg phosphatidylcholine and cholesterol (for injection) were obtained from AVT (shanghai) Pharmaceutical Tech Co., Ltd. Glutaraldehyde stationary liquid (2.5%) and 5,5',6,6'-tetrachloro-1,1',3,3'-tetraethylimidacarbocyanine (JC-1) assay kit were bought from Beijing Solarbio Science & Technology Co., Ltd. (Beijing, China). GSH assay kit (abs580006-96T) was purchased from Absin (Shanghai, China). Malonaldehyde (MDA) assay kit came from Jiancheng Bioengineering Institute (Nanjing, China). O58 probe was supplied by BestBio (Nanjing, China). C11-$BODIPY^{581/591}$ was obtained from Thermo Fisher Scientific Inc (MA, USA). FITC Rabbit anti-goat IgG (H + L) antibody (K1213) was from APExBIO (Houston, USA).

Cells and animals

Macrophage cell line (RAW 264.7), Lewis lung carcinoma line (LLC), and lung epithelial cell line (MLE-12) were provided by Shanghai Cell Bank, Chinese Academy of Sciences (Shanghai, China). RAW 264.7 cells, LLC cells, and LLC cells stably expressing firefly luciferase (LLC-Luc) were incubated at 37℃ in high glucose Dulbecco's medium (DMEM) medium (HyClone) containing 10% fetal bovine serum (FBS, Biochannel, BC-SE-FBS01), 100 U/mL penicillin, and 100 μg/mL streptomycin (Gibco). MLE-12 cells were maintained at 37℃ in DMEM/F12 supplemented with 5 μg/mL insulin, 10 μg/mL transferrin, 30 nM sodium selenite, 10 nM hydrocortisone, 10 nM β-estradiol, 2 mM L-glutamine, and 2% FBS.

Male C57B/6 (4 ~ 6 weeks) mice were purchased from the Laboratory Animal Center of Fudan University (Shanghai, China) and raised in specific pathogen-free conditions. All the mice were acclimated to environment for 7 days prior to experiments. All the animal experimental procedures were in accordance with the guidelines for the Care and Use of Laboratory Animals of Fudan University and approved by the Institutional Animal Care and Use Committee of the School of Pharmacy, Fudan University.

Isolation of RAW 264.7 cell membrane

RAW 264.7 cells in logarithmic growth phase were washed three times with pre-chilled PBS, harvested, and centrifuged to collect cell precipitation. According to the protocol of the membrane and cytosol protein extraction kit, cell precipitation was resuspended in reagent A containing 1 mM PMSF, placed in ice-water bath for 15 min, and homogenized 50 times by a pre-cold handheld glass homogenizer. The homogenate was then centrifuged (4 °C, 1000 g) for 10 min to remove cell nuclei and unbroken cells and the supernatant was then centrifuged (4 °C, 14000 g) for 0.5 h to pellet cell membrane fragments. After resuspending in PBS, the suspension was extruded through 800 nm and 200 nm porous polycarbonate filters for 11 times to prepare RAW 264.7 cell-membrane nanovesicles (RCM). The protein content of RCM was determined using a BCA assay kit.

Preparation of DHA-N@M

To investigate the optimal ratio, RCM and DHA-SNO were mixed in PBS at different weight ratios and incubated for 0.5 h in a 37 °C water bath to form DHA-SNO-inserted RCM nanoreactors (DHA-N@M), followed by wash with PBS to remove free DHA-SNO. After

extracting DHA-SNO with methanol from DHA-N@M, the encapsulation efficiency and drug loading efficiency were determined by high performance liquid chromatography (HPLC, Agilent 1260 infinity, USA) method: column, Eclipse Plus C18, 4.6 × 250 mm, 5 Micro; mobile phase, acetonitrile, tetrahydrofuran, and 0.4% acetic acid solution (77:3:20); flow rate, 1.0 mL/min; column temperature, 30 °C; sample volume, 18 μL; detection wavelength, 210 nm.

Characterization of DHA-N@M

The structure of RBC and DHA-N@M was observed using a Cryo-transmission electron microscopy (Cryo-TEM, Tecnai G2 F20, Fei, USA). The particle size, polydispersity index (PDI), and Zeta potential were measured by the dynamic light scattering (DLS) performed on the Zetasizer Nano ZS device. Fourier transform infrared spectroscopy (FT-IR, Nicolet™ iS5, Thermo Fisher Scientific Inc, USA) was employed to determine the functional groups of nanoreactors.

To test stability in typical storage condition, DHA-N@M was dispersed in PBS and stored at 4 °C. Daily measurements were carried out to monitor changes in particle size, PDI, and drug loading content after centrifugation to remove leak DHA-SNO. Additionally, the particle size of DHA-N@M incubated in PBS (pH 7.4) and PBS (pH 7.4) with 10% FBS after 24 h were determined to assess the stability in physiological fluid conditions.

The protein profiles in RAW 264.7, RCM, DHA-SNO, and DHA-N@M were determined by sodium dodecyl sulfate-polyacrylamide gel electrophoresis (SDS-PAGE) analysis. The typical markers of integrin α4 and CCR2 were identified by western blot analysis.

Next, we evaluated the GSH-responsiveness of DHA-N@M. DHA-N@M was respectively suspended in PBS (pH 7.4) and PBS (pH 7.4) + 10 mM GSH containing a NO fluorescent probe of DAR-1 (5 μM) with or without X-ray (6 Gy) and kept in a 37 °C shaker. The fluorescence values of the solution (Ex = 560 nm, Em = 595 nm) were measured at predetermined time points using a microplate reader (Synergy 2, BioTek Instruments Inc, USA). Furthermore, the morphology and the particle size of DHA-N@M were monitored after incubation in PBS (pH 7.4) and PBS (pH 7.4) + 10 mM GSH with or without X-ray (6 Gy).

The GSH consumption ability of DHA-N@M was determined using DTNB method. DHA-N@M was redispersed in PBS (pH 7.4) containing 10 mM GSH mimicking tumor intracellular high-reduction environment. After vibrating with shaker at 37 °C for 12 h, the supernatant was collected *via* centrifugation, reacted with DTNB, and the optical density (OD) at 405 nm was measured using a microplate reader.

Cellular uptake

The preparation of rhodamine-B-fluorescent-group-modified-DHA@M (D-RhB@M) was similar as that of DHA-N@M. For the stability test, D-RhB@M and DHA-N@M were incubated in cell culture media with or without 10%FBS, and cargo leakage was evaluated using spectrofluorometer or HPLC.

RAW 264.7 cells, LLC cells and MLE-12 cells were counted by automatic cell counter (Countstar BioTech, Shanghai, China) and seeded in confocal dishes with incubation overnight. Then the cells were incubated with free D-RhB and D-RhB@M with equal concentration of D-RhB for 4 h, rinsed three times with cold PBS to remove free drug, and visualized under confocal laser scanning microscopy (CLSM, LSM 710, Zeiss, Germany). Meanwhile, the treated cells were collected, made into single-cell suspension, and then subjected to flow cytometry (FCM) analysis (CytoFlex S, Beckman, USA) to quantify cellular uptake.

Three different DID-labeled nanovesicles were prepared as follow. (1) DID-labeled RCM (DID@M) was prepared as previously depicted and the stability test of DID@M was similar as that of D-RhB@M. (2) To confirm the role of integrin α4 of macrophage membrane in mediating cellular uptake, DID@M was mixed with anti-integrin α4 antibody, which was designated as the blocked DID@M group. (3) To further explore the superiority of RCM-based nanovesicles, liposome, a classical dosage form, was served as a formulation control. Egg phosphatidylcholine and cholesterol were dissolved at molar ratio of 60%/40% in 1 mL chloroform, and DID at 1% molar ratio was added. The mixture was evaporated to form a uniform blue film at the bottom of the round-bottom flask, which was then hydrated in 1 mL PBS, sonicated and passed repeatedly through a 200 nm porous polycarbonate filter to obtain the DID-labeled liposome (DID@Lipo) with equivalent particle size to DID@M. Following an overnight culture, the cells were respectively incubated DID@M, DID@Lipo, and blocked DID@M carrying equal fluorescence dye for 4 h. Nuclei were stained with DAPI and observed by CLSM.

In vitro cytotoxicity study

The viability of LLC cells was investigated by CCK-8 assay. In brief, LLC cells were seeded in 96-well plates at 10,000 cells/well and cultured overnight. Then, DHA, DHA@M, SNO-grafted behenic acid (BA-SNO), BA-N@M, DHA-SNO, and DHA-N@M with different concentrations were respectively added to the culture media for 12 h, while the cells in radiation groups were exposed to 6 Gy X-ray (RS 2000, Rad Source Technologies, USA). After culture for another 12 h, 10% CCK-8 solution was added to each well for 1 h incubation and the OD value at 450 nm was recorded by a microplate reader.

MLE-12 cells were used to assess the possible cytotoxicity of DHA-N@M on normal lung cells. Following overnight incubation to adherent, cells were treated with DHA-N@M at concentrations ranging from 1 μM to 100 μM for 24 h, and the cell viability was determined by CCK-8 assay.

To investigate the cell death pathway, various cell death pathway inhibitors were used to rescue cell death mediated by DHA-N@M + X-ray. In brief, LLC cells were seeded in 96-well plates and grown to 70 ~ 80% confluency. Then cells were exposed to X-ray (6 Gy) at 12 h of incubation with 50 μM DHA-N@M in the absence or presence of 25 μM Nec-1, 50 μM Z-VAD-Fmk, or 1 μM Fer-1. Another 12 h after cell culture, cell viability was determined using CCK-8 assay.

NO, ROS, and $ONOO^-$ production in LLC cells

To detect the intracellular NO, ROS, and $ONOO^-$, LLC cells were seeded in glass-bottom 24-well plates (NEST Biotechnology Co., Ltd, Wuxi, China) for CLSM imaging or 12-well plates for FCM analysis and cultured overnight prior to studies. DHA-SNO, DHA@M, BA-N@M, and DHA-N@M at 50 μM suspended in DMEM were added and incubation for 12 h. Afterwards, cells were loaded with probes at working concentration (NO probe: 3-amino-4-aminomethyl-2',7'-difluorescein diacetate, DAF-FM DA, at 5 μM; ROS probe: DCFH-DA at 10 μM; $ONOO^-$ probe: O58 at 1:1000) for 30 min, with a three-time wash using PBS to remove excess or non-specific probes and a replacement with fresh DMEM. Subsequently, cells in radiation groups were irradiated (6 Gy) and their nucleus were identified by Hoechst 33342 staining (10 μg/mL) for CLSM imaging.

Meanwhile, the cells following the same treatment were harvested, processed into single-cell suspensions, and subjected to FCM analysis to quantify the level of intracellular NO, ROS, and $ONOO^-$.

Detection of GSH and GPX4

LLC cells were at a density of 3×10^5 cells per well in 6-well plates. After incubation overnight and attachment, DHA-SNO, DHA@M, BA-N@M, and DHA-N@M at 50 μM were added and co-incubation with cells for 12 h, following with 6 Gy X-ray irradiation. Then cells were harvested 12 h post-culture, washed with PBS and lysed in lysis buffer containing 1 mM PMSF. GSH content in cell lysates were performed by the reduced GSH assay kit according to the instructions, which were normalized to total protein content using a BCA assay.

Additionally, after denaturation by boiling in loading buffer, the total protein in cell lysate was separated by 15% SDS-PAGE, transferred from gel to nitrocellulose membrane (Millipore, USA) at 250 mA for 2 h, and blocked with by 5% non-fat milk for 1 h. Subsequently, specific primary antibodies (rabbit anti-GPX4, dilution 1:1000; mouse anti-β-actin, dilution 1:1000) were added for overnight incubation at 4 °C and the antibody-bound proteins were developed with the enhanced chemiluminescence reagent coupled with horseradish peroxidase-conjugated secondary antibody.

Measurement of intracellular LPO and MDA formation

Next, the levels of LPO and MDA, as the characteristic indicators of ferroptosis, were estimated to reflect the effect of DHA-N@M + X-ray on ferroptosis. For LPO staining, LLC cells grown in confocal culture plates were incubate with different formulations including DHA-SNO, DHA@M, BA-N@M, and DHA-N@M for 12 h with or without X-ray exposure. After continuous culture for 12 h, 10 μM C11-$BODIPY^{581/591}$ staining was carried out for 0.5 h at 37 °C, protected from light. After Hoechst 33342 staining and wash steps, the intracellular oxidation of probe by LPO was visualized under CLSM.

Lysates from LLC cells treated with different formulations were prepared as described above and used for measuring MDA content in accordance with the kit instructions.

Mitochondrial membrane potential (ΔΨm) test

The change of ΔΨm is indicated by the green/red fluorescence intensity ratio of JC-1. LLC cells in logarithmic growth phase were seeded at a density of 1.2×10^5 cells/well in 24-well glass bottom confocal plates. After overnight incubation, various formulations were added: control medium, DHA-SNO, DHA@M, BA-N@M, and DHA-N@M. Cells in the radiation therapy group were incubated with the formulations for 12 h before receiving a single dose of X-ray irradiation. Following standard culture for an additional 12 h, JC-1 probe was added at the working concentration according to the kit instructions. After incubation at 37 °C in the dark for 0.5 h, cells were washed twice with pre-chilled staining buffer and then with Hank's buffer. Intracellular fluorescence was immediately observed using CLSM.

Observation of mitochondria morphology

Bio-TEM was applied to observe the morphology of mitochondria. After overnight cultivation in 10-cm dish, LLC cells were incubated with DMEM containing DHA-N@M at 50 μM for 12 h before being subjected to 6 Gy X-ray irradiation. In contrast, the untreated and unirradiated LLC cells were performed as control. Following an additional 12 h incubation, cells were collected using a cell scraper and centrifuged at 1500 rpm for 10 min to harvest cell pellet, which was then fixed with pre-cold 2.5% glutaraldehyde stationary liquid. After overnight fixation at 4 °C, the cell samples were processed as the standard sample preparation and bio-TEM observation.

DNA damage evaluation

Immunofluorescence assay for γ-H2AX was performed to assess the DNA damage. LLC cells were incubated with different formulations for 12 h without or with X-ray irradiation. One hour after X-ray treatment, cells were fixed with 4% paraformaldehyde for 15 min at room temperature. After being rinsed with PBS, buffer supplemented with 5% BSA and 0.3% Triton X-100 was used to block and permeabilize. Next, cells were incubated overnight at 4 °C with rabbit anti-γ-H2AX (1:200). After washing, the secondary antibody with FITC labeling was added for 1 h followed by nuclear DAPI counterstain and CLSM observation.

Target lipidomics study

Target lipidomics study was performed by Shanghai Bioprofile Technology Co., Ltd. In detailed, LLC cells were exposed to 6 Gy X-ray after a 12-hour incubation with DHA-N@M. Cells without treatment were taken as the control. All cells were washed, collected with scrapers, counted, and centrifuged. The obtained cell samples were subjected to extraction by adding 200 μL of pre-chilled 75% methanol solution and 825 μL tert-butyl methyl ether (MTBE), followed by shaking for 60 min. Subsequently, the samples were sonicated in an ice-bath for 30 min, then 200 μL of water was added and mixed, followed by incubation at room temperature for 10 min. After centrifugation at 4 °C and 16,000 g for 20 min, the precipitated proteins were resuspended in 300 μL of SDT buffer. The solution containing an equal number of cells was subjected to vacuum drying, reconstituted in 120 μL of DCM/methanol (1:1, v/v), centrifugated to collect supernatant for UPLC-MS/MS analysis. Of note, the sample processing was conducted at 4 °C throughout.

Samples were separated by ultra high-performance liquid chromatography (UPLC; Nexera X2 LC-30AD, Shimadzu) on an Acquity UPLC BEH HILIC column (130Å, 1.7 μm, 2.1 mm × 100 mm, Waters) column followed by mass spectroscopy performed on QTRAP 5500 (AB SCIEX). Mobile phase A (water/acetonitrile (50:50, v/v) with 10 mM ammonium acetate, pH 8.0) and mobile phase B (acetonitrile) were used for gradient elution: 0–0.1 min, 85% mobile phase B; 0.1–7.5 min, a linear gradient of B from 85 to 65%; 8.5–11 min, a linear gradient of B from 65 to 5%; 11–11.1 min, a linear gradient of B from 5 to 85%; 11.1–15 min, 85% mobile phase B. Flow rate, 300 μL/min; Column temperature, 40 °C; Sample volume, 2 μL; Sample temperature, 4 °C.

Electrospray ionization conditions in positive ion mode: Source Temperature 550℃, Ion Source Gas1 (GAS1): 40, Ion Source Gas2 (GAS2): 50, Curtain Gas (CUR): 35, Ion Spray Voltage Floating (ISVF) 5500 V.

Electrospray ionization conditions in negative ion mode: Source Temperature 550℃, Ion Source Gas1 (GAS1): 40, Ion Source Gas2 (GAS2): 50, Curtain Gas (CUR): 35, Ion Spray Voltage Floating (ISVF) -4500 V.

Assessment on the feasibility of RCM inhalation

The particle size, PDI, and the DHA-SNO leakage of DHA-N@M before and after aerosolization by liquid aerosol device (HY-LWH03, YSKD bio-technology co., LTD, China) consisted of a micro-sprayer and a high-pressure syringe.

A next-generation impactor (NGI; Copley Scientific, UK) was employed to analyze the aerosol particle size distribution (APSD). The flow rate was set to 15 L/min (± 5%) and the experiment was performed in an NGI cooler at 5 ± 1.5 °C with at least 90 min pre-cooling time. DHA-N@M solution was loaded into the nebulizer cup, and the apparatus was assembled according to the manufacturer's instructions, followed by simultaneous activation of the flow pump and nebulizer (PARI Turboboy N compressor/LC Plus nebulizer, PARI GmbH, Starnberg, Germany). Upon completion of nebulization, nanoreactors deposited in the induction port and impaction cups were respectively collected for HPLC quantification. APSD parameters, including fine particle fraction (FPF), mass median aerodynamic diameter (MMAD), and geometric standard deviation (GSD), were calculated by Copley Inhaler Testing Data Analysis Software (version 3.10 EIBU).

Under cold light source, locating the glottis of mice using a small animal Laryngoscope (HY-SHJ01, YSKD bio-technology co., LTD, China). Then the liquid aerosol device was inserted into the trachea *via* the oral cavity and glottis, and immediately 25 μL of Evans Blue was spayed into lungs. Afterwards, the mice were transcardially perfused with 0.9% NaCl (15 mL), after which lungs were excised to observe distribution of the blue dye.

Orthotopic lung cancer model

LLC-Luc cells were resuspended in PBS to a concentration of 6.6×10^5 cells/mL and mixed with an equal volume of GelNest™, kept on ice-water bath to maintain cell viability and fluidity of GelNest™. C57BL/6 mice were anesthetized, shaved, and a small skin incision was made on the left chest to expose lungs. About 10^5 cells in 30 μL suspension were injected into the left lung to a depth of 4 mm, followed by immediate surgical glue (3M, USA) application to stitch the incision. After inoculation, the mice were placed at the right lateral decubitus position in a heating pad and monitored until fully awaken from narcosis. The tumor burden was recorded based on luciferase bioluminescence.

Biodistribution study

The biodistribution experiment was carried out in orthotopic LLC-Luc tumor bearing mice, who were randomly

divided into three groups (three mice per group). The mice were i.t. administered with DID@M or DID@Lipo, or i.v. injected with DID@M at an equal dose of 0.2 mg/kg of DID. At 6, 12, 24, and 48 h post-administration, mice were received intraperitoneal injection of D-luciferin potassium salt at 150 mg/kg and euthanized 12 min later. The heart, liver, spleen, lung, kidney, and blood samples (20 μL) were collected for fluorescence imaging (IVIS Spectrum, USA).

To determine the localization of nanovesicles in orthotopic lung tumors, the lung tissues with tumors were excised at 12 h after administration, rapidly frozen, optimal cutting temperature (OCT)-embedded, and cryosectioned. After the slides were counterstained by DAPI to visualize nuclei, the microscopic distribution of DID-labeled nanovesicles in lung and tumor was observed using CLSM.

In vivo therapy

The therapeutic efficacy of DHA-N@M mediated ferroptosis-radiotherapy was examined in orthotopic LLC-Luc lung cancer model. Five days after tumor cell inoculation (set as Day 0), the tumor-bearing mice were randomly divided into seven groups (Day 0) and respectively i.t. injection with 25 μL of PBS (G1), DHA-N@M (G2), PBS (G3), DHA-SNO (G4), DHA@M (G5), BA-N@M (G6), and DHA-N@M (G7) at 7.5 μmol/kg (Day 1). Of these, mice in G3 ~ G7 were received a single dose of 6 Gy X-ray 12 h after nebulization. During irradiation, mice were with a small animal gas anesthesia machine (ABS, Yuyanbio) and placed in a dedicated container for local irradiation while lying on their right side. A lead plate covered other parts of the mice, exposing only the lung region. The treatment was repeated on Day 7.

The mice were weighted every 2 days and bioluminescence-imaged to monitor the tumor progression on Day 0, 3, 6, 9, 12, 15, and 20. The relative tumor progression was normalized to the initial total flux on Day 0. The tumor inhibition rate was calculated as follows:

$$\text{Tumor inhibition rate}=1-\frac{\text{Relative tumor total flux(treatment)}}{\text{Relative tumor total flux(control)}}$$

On Day 20, the mice were sacrificed to collect the heart, liver, spleen, lung with tumor, kidney, and trachea. The lungs with tumors were prepared for hematoxylin and eosin (H&E) staining to observe the tumor cellularity. H&E staining was also applied on the other organs to preliminarily evaluate systemic toxicity of the treatment regimen.

Immunofluorescence staining

LLC-Luc tumor-bearing mice were treated as described above. One day (24 h) after the last X-ray irradiation, the lungs with tumors were excised to prepare paraffin-embedded sections which were stained with antibodies or probe (anti-GPX4, dilution 1:600; anti-3-NT, dilution 1:200; anti-γ-H2AX, dilution 1:1000; C11-BODIPY$^{581/591}$).

Statistical analysis

Data were presented as mean ± standard deviation (SD). Student's t-test, one-way ANOVA, or two-way ANOVA was used to determine statistical significance. *n.s.* means no significance, and the difference was considered significant as $^{*}P<0.05$, $^{**}P<0.01$, and $^{***}P<0.001$.

Results

Preparation and characterization

DHA-N@M was prepared in three steps (Fig. 2A): (1) Synthesizing DHA-SNO (**Fig. S1 ~ S10**); (2) isolating the cell membranes of macrophage cell line (RAW 264.7) with reference to published method [21], and extruding them to prepare RCM; (3) incubating DHA-SNO with RCM for 30 min, after which DHA-SNO would be spontaneously incorporated onto RCM due to its lipid tether structure [22, 23]. For comparison, a SNO-grafted saturated fatty acid (BA-SNO) was synthesized (**Fig. S11 ~ S17**), and the insertion of DHA or BA-SNO into the RCM was also performed following the same procedure described for DHA-N@M to fabricate DHA@M or BA-N@M, respectively. The ratio of DHA-SNO to RCM was optimized by striking a balance between encapsulation efficiency and drug loading content, with a 2:1 ratio optimal (**Table S1**). The DLS analysis showed that the hydrodynamic diameter was 113.3 ± 18.170 nm with a PDI of 0.146 for RCM and 121.6 ± 9.725 nm with a PDI of 0.224 for DHA-N@M (Fig. 2B). The Zeta potential value was changed from -29.7 ± 5.92 mV for RCM to -33.6 ± 1.27 mV for DHA-N@M (**Fig. S18**), and the negative charge of nanovesicles indicated the right-side-out orientation of cell membrane [24], facilitating the preservation of its biological properties. RCM presented a typical membranous vesicle morphology in Cryo-TEM, while DHA-N@M maintained a spherical morphology but exhibited discontinuity in the membrane layer (Fig. 2B). The PUFA absorption peak at 3012 cm^{-1} appeared in FT-IR spectra of DHA-N@M, suggesting the successful incorporation of DHA-SNO into RCM (**Fig. S19**). SDS-PAGE revealed that DHA-N@M's protein profile closely matched RCM but differed from cell lysates (**Fig. S20**). In addition, the specific proteins integrin α4 and CCR2 of macrophage cells were well-retained in DHA-N@M, while the nearly invisible of β-actin signals in RCM and DHA-N@M confirmed the highly purified of the cell membranes (Fig. 2C). All these data validated the development of DHA-N@M by inserting DHA-SNO into the RCM, endowing DHA-N@M with the tumor-tropism

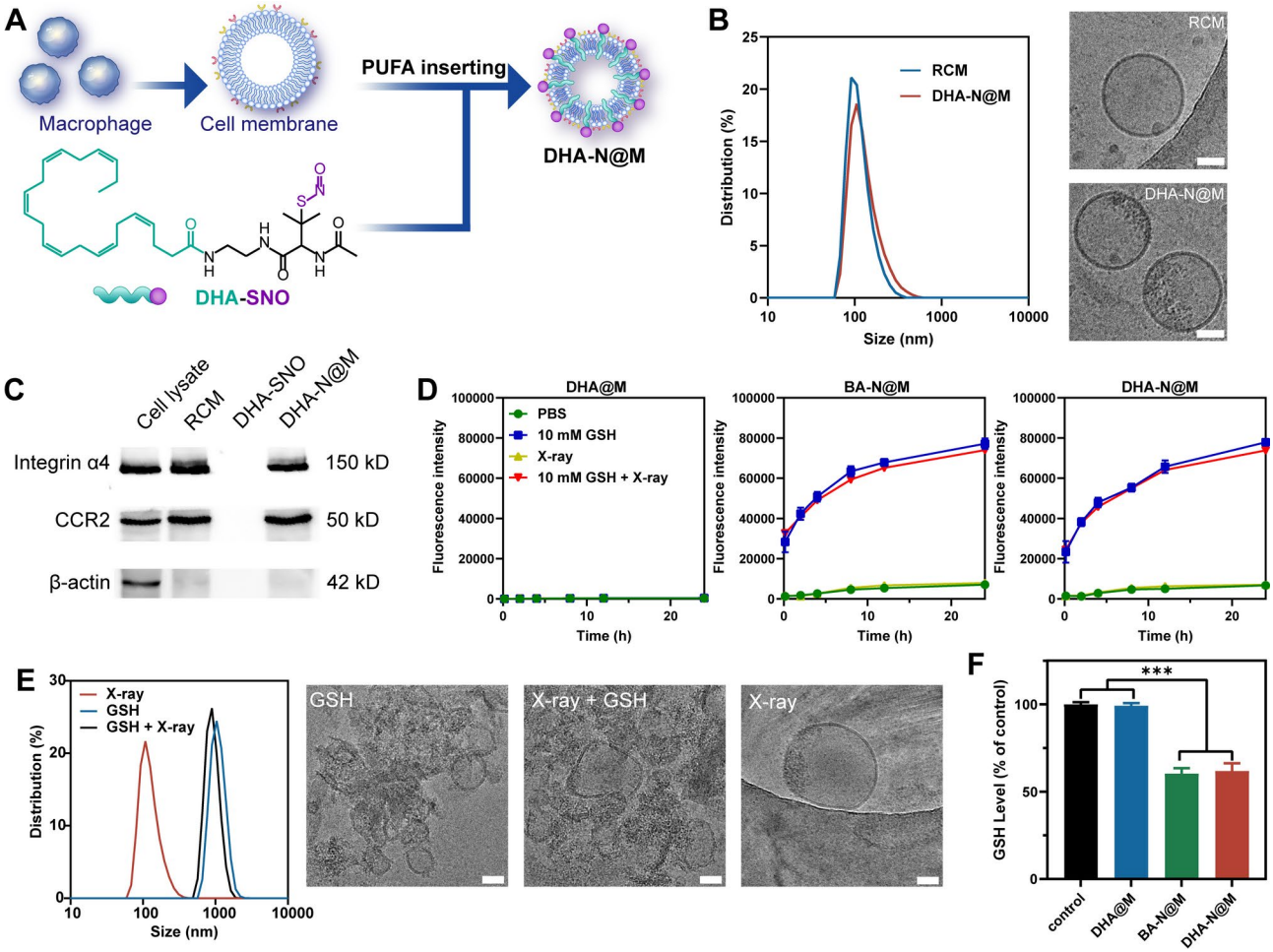

Fig. 2 Characterization of DHA-N@M. (**A**) Schematic illustration of DHA-N@M preparation (Created by FigDraw). (**B**) Size distribution and Cryo-TEM of RCM and DHA-N@M. (**C**) Typical protein markers of integrin α4, CCR2, and β-actin by western blot analysis. (**D**) NO release from DHA@M, BA-N@M, and DHA-N@M during different conditions ($n = 3$). (**E**) Size distribution and Cryo-TEM of DHA-N@M at different conditions. (**F**) GSH consumption in the solution after incubation with DHA@M, DHA-N@M and BA-N@M ($n = 3$)

potentiality to facilitate the high tumor accumulation. Moreover, there was no obvious variation in diameter, PDI, drug loading of DHA-N@M at daily storage condition and in the mimicked physiological fluids (**Fig. S21**), indicating agreeable stability for future studies.

Under GSH-reduction, the S-N bonds of two molecules of SNO would homolyze, resulting in two molecules of NO release and one molecule of oxidized GSH (GSSG) generation [25, 26]. Therefore, we investigated the GSH-responsive NO release profile of DHA-N@M in PBS (pH 7.4) containing 10 mM GSH in absence or presence of X-ray (6 Gy) using a classic NO probe of DAR-1. As shown in Fig. 2D, the fluorescence signals of DHA@M at any conditions were not detected as clearly. In the GSH-containing media, the DHA-N@M and BA-N@M gave off obvious fluorescence signals of NO, which increased over time and reached a relatively plateau after 12 h, while only slight NO leakage was observed upon their incubation in PBS. Meanwhile, the introduction of X-ray did not alter the NO release profile of DHA-N@M and BA-N@M, indicating that the low dose of X-ray used in this study was insufficient to break the S-N bond. Likewise, at GSH solution, DLS analysis showed that obvious aggregation occurred, and the spherical morphology of DHA-N@M was disrupted into membrane fragments observed by Cryo-TEM, while X-ray radiation had no effect (Fig. 2E). Next, the GSH depletion capacity was measured *via* DTNB method (Fig. 2F). Due to the equal amounts of SNO, the GSH consumption abilities of the DHA-N@M and BA-N@M were comparable and significant, reducing ~ 40% GSH. These results suggested that the GSH-responsive property of DHA-N@M enable tumor-specific activation during nebulization and X-ray irradiation, thereby minimizing off-target toxicity in normal tissues.

Cellular uptake and in vitro anticancer activity

The cellular uptake of nanovesicles was investigated in LLC, RAW 264.7, and MLE-12 cells. The high expression on VCAM-1 on LLC cells was validated (**Fig. S22**). To evaluated the uptake difference between free-PUFA and nanovesicle, D-RhB was synthesized, and then, D-RhB@M and DID@M were prepared as the procedure described for DHA-N@M (**Fig. S23**~**S25**). Before cellular uptake assays, we confirmed minimal cargo leakage from DHA-N@M, D-RhB@M, or DID@M over 72 h in both serum-free and 10% FBS-supplemented cell culture media, ensuring that the observed fluorescence signals in uptake study would accurately reflect nanovesicle internalization profile rather than free dye (**Fig. S26**). As displayed in Fig. 3A and **S27**, the fluorescence from D-RhB in RAW 264.7 or MLE-12 cells was significantly brighter than that of D-RhB@M, while D-RhB@M showed an enhancement of cellular uptake by LLC cells over D-RhB. Additionally, similarly sized DID@Lipo was prepared to demonstrate superiority of membrane-based nanovesicle over existing agent. The uptake of DID@M in LLC cells was 1.9 times that of DID@Lipo and reduced by 40.23% after integrin α4 being blocked (Fig. 3B and **S28**). Compared with liposome, the uptake of DID@M by macrophage cells was dramatically decreased. The weak fluorescent signals in MLE-12 cells, either in DID@Lipo or DID@M group, indicated the lower uptake of nanoscopic-size formulations by MLE-12 cells. All the above results confirmed that membrane-based nanovesicles exhibited enhanced cellular uptake in LLC cells mediated by integrin α4 [27], and effectively escaped from phagocytosis by macrophages due to the invisibility-cloak effect of the natural macrophage membrane associated proteins [28].

The i*n vitro* radiotherapeutic inhibitory activity of DHA-N@M was analyzed in LLC cells (Fig. 3C). 6 Gy of X-ray alone induced cell death in 22.29 ± 2.87%, which did not be enhanced by DHA@M at 0.5 μM ~ 50 μM but slightly increased to 38.45 ± 3.45% combined by 100 μM DHA@M. Treatment with DHA-N@M above 50 μM reduced the viability of LLC cells, combination treatment with X-ray further inhibited cell survival to 21.67 ± 1.63% at 50 μM and 2.15 ± 0.43% at 100 μM, which was stronger than that of free DHA-SNO due to the higher cellular uptake mediated by RCM. Meanwhile, the relatively stronger radiotherapeutic effect of DHA-N@M compared to BA-N@M emphasized the importance of PUFA in synergistic treatment strategy. The combination index (CI) of DHA-N@M (10, 50, and 100 μM) + X-ray were 1.00927, 0.83978, and 0.56767, where value less than 0.9, between 0.9 ~ 1.1, or greater than 1.1 represents synergistic, additive, or antagonistic effects, respectively, indicating DHA-N@M acted synergistically with radiotherapy (**Fig. S29**) [29]. As shown in **Fig. S30**, the DHA-N@M was almost harmless to MLE-12 cells at the concentration range of 0.5 μM ~ 50 μM, while a suppressive cell growth was observed upon 100 μM DHA-N@M incubation. Consider both the cytocompatibility in normal cells and the cytotoxicity in tumor cells, the DHA-N@M concentration was kept at 50 μM in the subsequent cell studies. To determine the cell death pathway activated by DHA-N@M + X-ray, the rescue abilities of different cell death inhibitors were evaluated (Fig. 3D). The ferroptosis inhibitor (Fer-1) significantly blocked DHA-N@M + X-ray-mediated cell death, which predominated over the apoptosis inhibitor (Z-VAD-Fmk) and the necrosis inhibitor (Ner-1), suggesting the major role of ferroptosis.

Reinforcement on oxidative stress and disruption of redox homeostasis

To elucidate the mechanism underlying the enhanced radiotherapeutic effect of DHA-N@M, we performed cytological experiments in LLC cells. The cellular NO, ROS, and $ONOO^-$ were detected by commercially available probes, DAF-FM DA, DCFH-DA, and O58, respectively. As shown in Fig. 3E and S31, fluorescence was nearly absent in DHA@M-treated cells, in contract, the fluorescence intensities were nearly the identical in DHA-N@M, BA-N@M + X-ray, and DHA-N@M + X-ray groups for carrying the same amount of SNO, which was brighter than that in free DHA-SNO group due to the uptake difference. As expected, X-ray irradiation slightly increased the cellular ROS formation, and a visibly green fluorescence was observed in DHA-N@M-treated cells, as a result of the oxidation of NO to DCFH-DA (Fig. 3F and S32) [30, 31]. Of note, the cells treated with DHA-N@M + X-ray and BA-N@M + X-ray emitted strongest green fluorescence representing ROS, primarily due to the oxidation effect of NO on the probe and the consumption of GSH by SNO, which promoted the accumulation of ROS. As depicted in Fig. 3G and S33, the $ONOO^-$ production, formed by the reaction of ROS and NO, demonstrated the same tendency with cellular NO. Without mediation of NO, no $ONOO^-$ (red fluorescence) was detected in LLC cells exposed with X-ray or DHA@M + X-ray. DHA-N@M-treated cells showed a brighter fluorescence due to the small amounts of NO in tumor cells [32]. After X-ray exposure, the fluorescence was intensified in both BA-N@M + X-ray and DHA-N@M + X-ray groups, reaching about 1.7-fold that of the DHA-N@M group. All these results demonstrated DHA-N@M + X-ray caused heightened oxidative stress in LLC cells.

The redox system, especially GSH/GPX4, plays a negative role in ferroptosis. Upon incubation with DHA-N@M, the cellular GSH level decreased significantly by 31.09 ± 2.35% ($p < 0.01$), which was attributed to GSH

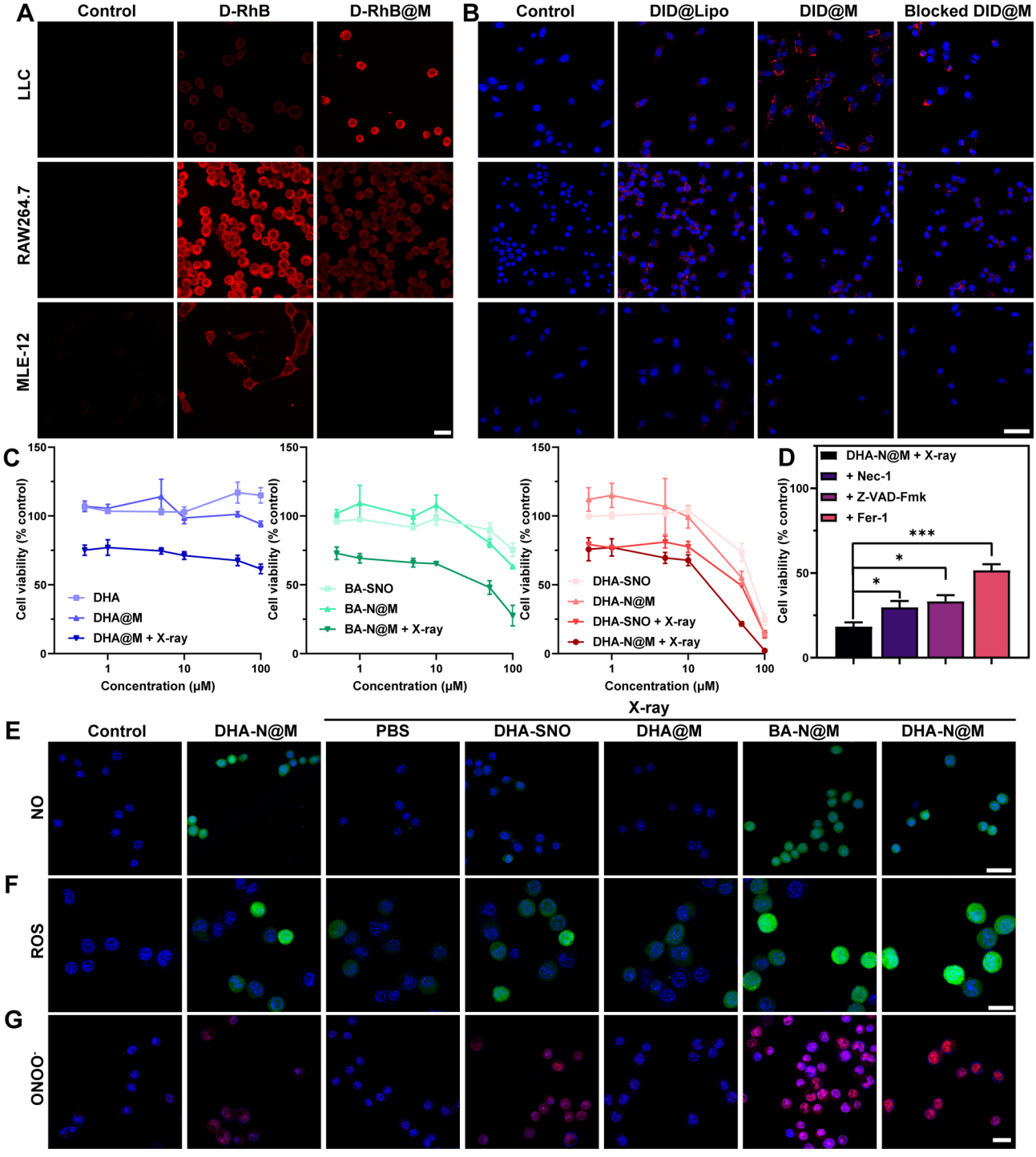

Fig. 3 Cellular uptake, cytotoxicity, and in vitro NO, ROS, and $ONOO^-$ generation. (**A**) CLSM images of LLC cells, RAW264.7 cells and MLE-12 cells after incubation with D-RhB or D-RhB@M. Scale bar = 20 μm. (**B**) CLSM images of LLC cells, RAW264.7 cells and MLE-12 cells after incubation with DID@Lipo, DID@M, and blocked DID@M. Scale bar = 50 μm. (**C**) Relative viability of LLC cells after different treatments ($n = 3$). (**D**) Relative viability of LLC cells treated with 50 μM DHA-N@M + 6 Gy X-ray in the presence of 25 μM Nec-1, 50 μM Z-VAD-Fmk, or 1 μM Fer-1 ($n = 3$). * and *** denote $p < 0.05$ and $p < 0.001$, respectively. CLSM images of (**E**) NO, (**F**) ROS, and (**G**) $ONOO^-$ in LLC cells after different treatments. Scale bar = 20 μm

mediating the cleavage of the S-N bond of DHA-N@M, resulting in substantial GSH consumption during this reaction (Fig. 4A). Unlike the comparable GSH consumption observed in solution, the cellular GSH depletion in DHA-N@M and BA-N@M + X-ray groups was inferior to that in DHA-N@M + X-ray group. The discrepancy may stem from the complex redox microenvironment in tumor cells, where $ONOO^-$ could denature intracellular GSH-related reductases and consequentlty inhibit GSH levels [33]. Additionally, compared to BA, the PUFA property of DHA facilitated the generation of LPO, leading to GSH consumption. These factors contributed to the most effective depletion of GSH in LLC cells by DHA-N@M + X-ray (40.97 ± 1.68%). Concomitant with GSH depletion, cellular GPX4 was dramatically inactivated with DHA-N@M + X-ray with a 57.20 ± 4.81% decline (Fig. 4B and S34). At this point, the balance of redox system had been broken by DHA-N@M + X-ray and tipped in favor of ferroptosis.

Afterwards, LPO and its final product MDA, as ferroptosis biomarkers, were analyzed. As shown in Fig. 4C and S35, the slightly increased ratio between the green signal and red signal in BA-N@M + X-ray group revealed that $ONOO^-$, as a potent oxidant, could induced LPO formation to some extent. Among all groups, the cells treated with DHA-N@M + X-ray exhibited the strongest green fluorescence and the weakest red fluorescence, with the ratio being 30.78-fold that of in X-ray and being 5.69-fold that of in BA-N@M + X-ray, indicating overwhelming LPO accumulation, which was attributed to the disruption of the GSH/GPX4 reductive defense system and the oxidative action of ROS/$ONOO^-$ on exogenous supplemented DHA. The levels of MDA presented the same trend, which was most abundant in DHA-N@M + X-ray group with a 165% increment (Fig. 4D).

Ferroptosis, $ONOO^-$, and excessive ROS have all been reported to associated with functional impairment of mitochondria [34, 35]. The JC-1 dye was applied to label ΔΨm to assess the degree of mitochondrial damage, where red fluorescence indicates healthy status at high ΔΨm, while green fluorescence represents dysfunctional mitochondria with low ΔΨm. As shown in Fig. 4E and S36, due to the action of NO, LLC cells treated with DHA-N@M exhibited slight but significant mitochondrial damage, with a higher ratio of green/red fluorescence signal compared to the control group ($p < 0.001$). In the BA-N@M + X-ray group, both $ONOO^-$ and ROS led to the presence of JC-1 dye predominantly in its green monomeric form, indicating mitochondrial damage. In the DHA-N@M + X-ray group, cells showed intense green fluorescence, with the ratio of green/red fluorescence signal being 52.58, 8.61, 23.59, 10.23, 31.76, and 3.30 times higher than that in G1 to G6, respectively ($p < 0.001$), indicating that the combined radiotherapy effect of DHA-N@M resulted in highly negative ΔΨm and severe mitochondrial damage. Additionally, it was observed by Bio-TEM that, different from control cells with intact mitochondrial morphology, mitochondria in LLC cells treated with DHA-N@M + X-ray presented a ferroptosis-associated morphological changes, including shrinkage, increased membrane density, reduced cristae, and outer membrane rupture (Fig. 4F) [36]. Based on the direct DNA damage ability of radiotherapy and the DNA fragmentation induce by $ONOO^-$ [37, 38], we conjectured the augment effect of DNA damage from DHA-N@M, which was verified by γ-H2AX immunofluorescence staining (Fig. 4G and S37). Under the combine action of radiotherapy and $ONOO^-$, there was 1.95-fold increase in green fluorescence in BA-N@M + X-ray group than that in X-ray group. Remarkably, DHA-N@M + X-ray group boost the most drastic DNA impairment by 8.79-fold than X-ray group, consistent with the notion that the aldehydic products generated from LPO during DHA-N@M + X-ray-mediated ferroptosis could form DNA adducts resulting in augment of DNA damage [39–41]. Taken together, DNA-N@M + X-ray induced ferroptosis *via* promotion of ROS/$ONOO^-$, downregulation of GSH/GPX4, and PUFA supplementation, causing severe DNA and mitochondrial damage.

Disturbance in lipid metabolism homeostasis

Given that PUFA supplementation changes cellular lipid composition and thereby controls the sensitivity to ferroptosis [42, 43], targeted lipidomics analysis was performed to elucidate the effect of DHA-N@M + X-ray on intracellular lipid composition and metabolism. In total, 958 lipid species were quantified. Principal component analysis (PCA score plot) and orthogonal partial least squares discriminant analysis (OPLS-DA) of extracted lipid metabolites exhibited a clear separation between two groups, with the control group gathering in the positive direction while the DHA-N@M + X-ray group clustering in the negative direction (Fig. 5A and B). With $|\mathrm{Log_2(fold\ change)}| > \mathrm{Log_2}1.5$ and $p < 0.05$ as the screening criterion, 398 significantly changed lipid species were discovered (Fig. 5C). Previous studies suggested that ferroptosis is executed by peroxidizing PUFA-chains-containing phospholipids (PL), especially phosphatidylethanolamines (PE) and phosphatidylcholines (PC) [44], while the lysophospholipids (LP) increase upon ferroptosis inducer treatments as the product of enzymatic cleavage of the oxidized PUFA tail [45, 46]. The majority of PUFA, PE-PUFA, PC-PUFA, and LP were upregulated after DHA-N@M + X-ray treatment (Fig. 5D, 5E, 5F, and 5G). Among the significantly changed lipid species, those containing monounsaturated fatty acids (MUFA) chains and saturated fatty acids (SFA) chains showed a downregulated trend,

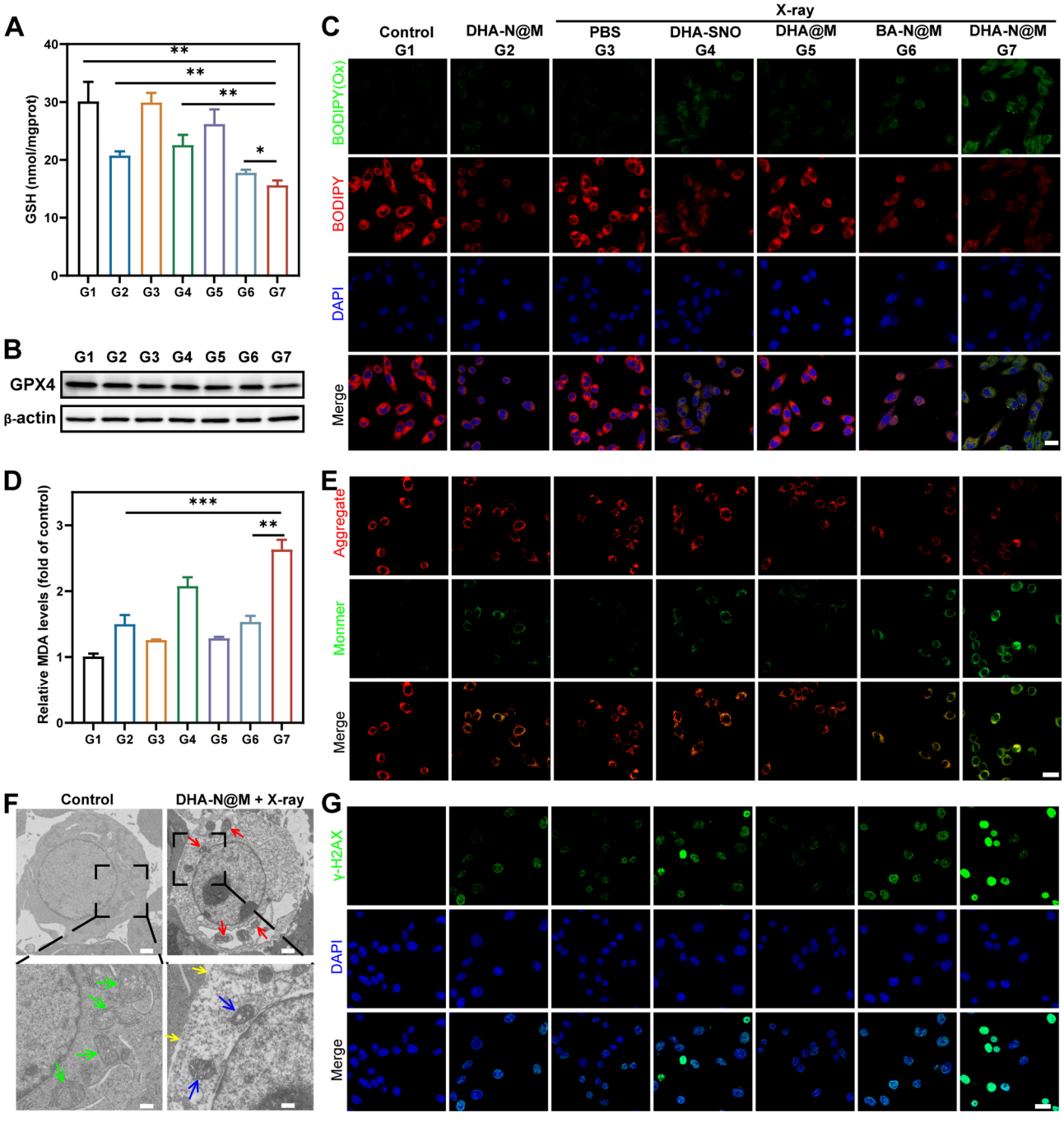

Fig. 4 The therapeutic mechanism of DHA-N@M upon X-ray irradiationin vitro. (**A**) GSH contents normalized to the total protein concentration in LLC cells after different treatments ($n = 3$). (**B**) Cellular protein expression of GPX4 in LLC cells after different treatments. (**C**) Determination of LPO generation in LLC cells after different treatments based on CLSM. Scale bar = 20 μm. (**D**) Relative MDA contents in LLC cells after different treatments ($n = 3$). (**E**) CLSM images of LLC cells after different treatments tested using JC-1 fluorescent probe. Scale bar = 20 μm. (**F**) Bio-TEM images and enlarged view of LLC cells. Green arrowheads indicate healthy mitochondria, red arrowheads point to the shrunken mitochondria with increased membrane density, blue arrowheads indicate disrupted outer mitochondrial membranes, and yellow arrowheads point to rupture of cell membranes. Scale bar = 1 μm for upper panel and 400 nm for lower panel. (**G**) CLSM images of LLC cells after different treatments immunostaining for γ-H2AX; Scale bar = 20 μm.*, **, and *** denote $p < 0.05$, $p < 0.01$ and $p < 0.001$, respectively

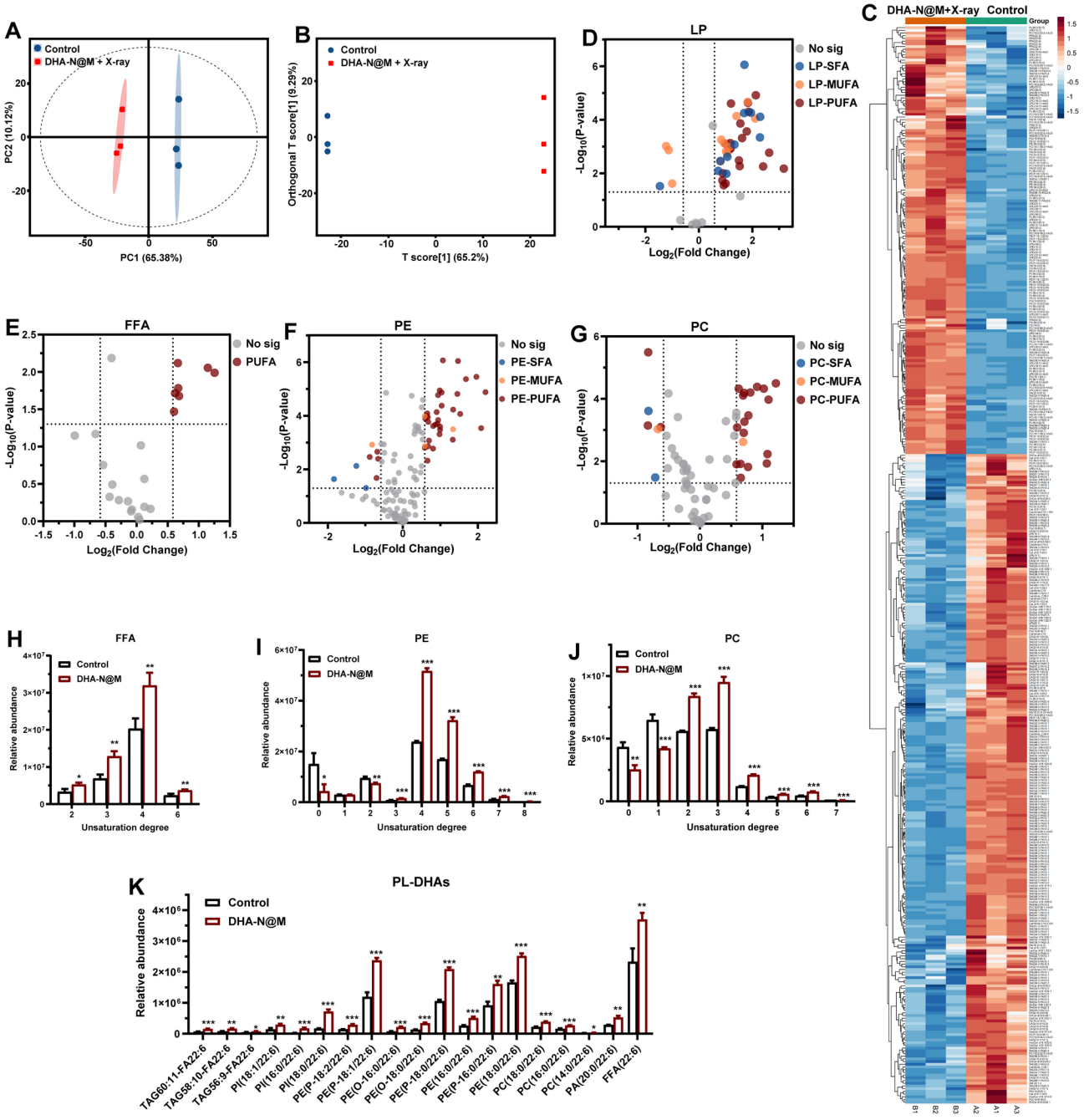

Fig. 5 Perturbation of lipid metabolism homeostasis by DHA-N@M upon X-ray irradiation. **(A)** PCA and **(B)** OPLS-DA plots of extracted lipid profiles of control and DHA-N@M + X-ray-treated cells. **(C)** Heatmap showing the significantly changed lipid abundances in control and DHA-N@M + X-ray-treated cells. Volcano plots representing the changes in **(D)** LP, **(E)** free fatty acid (FFA), **(F)** PE, and **(G)** PC. Quantification of the relative abundance of significantly changed **(H)** FFA, **(I)** PE, **(J)** PC with different unsaturation degrees in control and DHA-N@M + X-ray-treated cells ($n = 3$). **(K)** Quantification of the relative abundance of significantly changed PL-DHA in control and DHA-N@M + X-ray-treated cells ($n = 3$). *, **, and *** denote $p < 0.05$, $p < 0.01$ and $p < 0.001$, respectively

while those with high unsaturated degree exhibited a significantly increase (Fig. 5H, 5I, and 5J). Of note, Fig. 5K revealed the noticeable elevations of DHA across various PL. To summarize, these results showed that DHA-N@M + X-ray treatment increased the level of PUFA-containing lipids, resulting in the perturbation of lipid metabolic homeostasis and the amplification of ferroptosis.

Biodistribution of RCM *via* intratracheally administration

Before initiating the animal experiments, it is necessary to evaluate the feasibility of aerosolization of RCM and

the construction on orthotopic C57BL/6 murine model of lung tumor. As shown in **Fig. S38**, after nebulization by liquid aerosol device, the particle size of DHA-N@M slightly decreased from 121.6 ± 9.725 to 102.6 ± 3.428 nm maintaining a narrow size distribution with a constant PDI of 0.140 ± 0.003. The DHA-SNO content was marginally reduced to 93.35% of the pre-aerosolization value. Despite some minor variations, the structural integrity of the nebulized nanoreactors remained intact, with DHA-SNO leakage within the acceptable range. These results confirmed the tolerance of nanoreactor to the high pressure and shear forces generated by lipid aerosol device owing to the flexible structure of RCM [47, 48]. To assess pulmonary delivery efficiency, the APSD of DHA-N@M was measured *via* NGI and the deposition profile at various stages are as shown in **Fig. S39**. FPF, representing the percentage of particles with aerodynamic diameters ≤ 5 μm that can deposit in the lower respiratory tract [49], was measured at 77.80 ± 4.20%. MMAD, corresponding to the median diameter in the cumulative mass distribution, was 3.41 ± 0.11 μm, falling within the optimal 1–5 μm range for effective deposition in small airways and alveoli [49, 50]. GSD of 1.69 ± 0.14 further confirmed the favorable aerosol dispersion characteristics. These results collectively demonstrated that DHA-N@M exhibited both high FPF and optimal MMAD, ensuring efficient deep lung delivery while minimizing oropharyngeal deposition, thereby confirming its suitability as an excellent pulmonary delivery carrier. As shown in **Fig. S40**, homogeneous distribution of Evans blue administered by aerosolization was seen in the left and the right lung. These results demonstrated the feasibility of in vivo therapy with inhalable RCM. 5 days after orthotopic inoculation of LLC-Luc tumor cells, a single tumor nodule was observed both in macroscopic appearance and H&E stained image, with a single bioluminescence spot under IVIS system (**Fig. S41**), confirming the successful construction of orthotopic lung cancer model within 5 days.

To investigate the biodistribution of RCM, orthotopic LLC-Luc tumor-bearing mice were received i.t. or i.v. with DID@M or DID@Lipo with equal amount of fluorescent dye. The ex vivo fluorescence images were depicted in Fig. 6A, indicating DID@M injected i.v. primarily distributed in livers and spleens, which would result in suboptimal tumor accumulation and consequent compromise treatment effectiveness. Both inhaled DID@M and DID@Lipo exhibited preferential enrichment at lung over

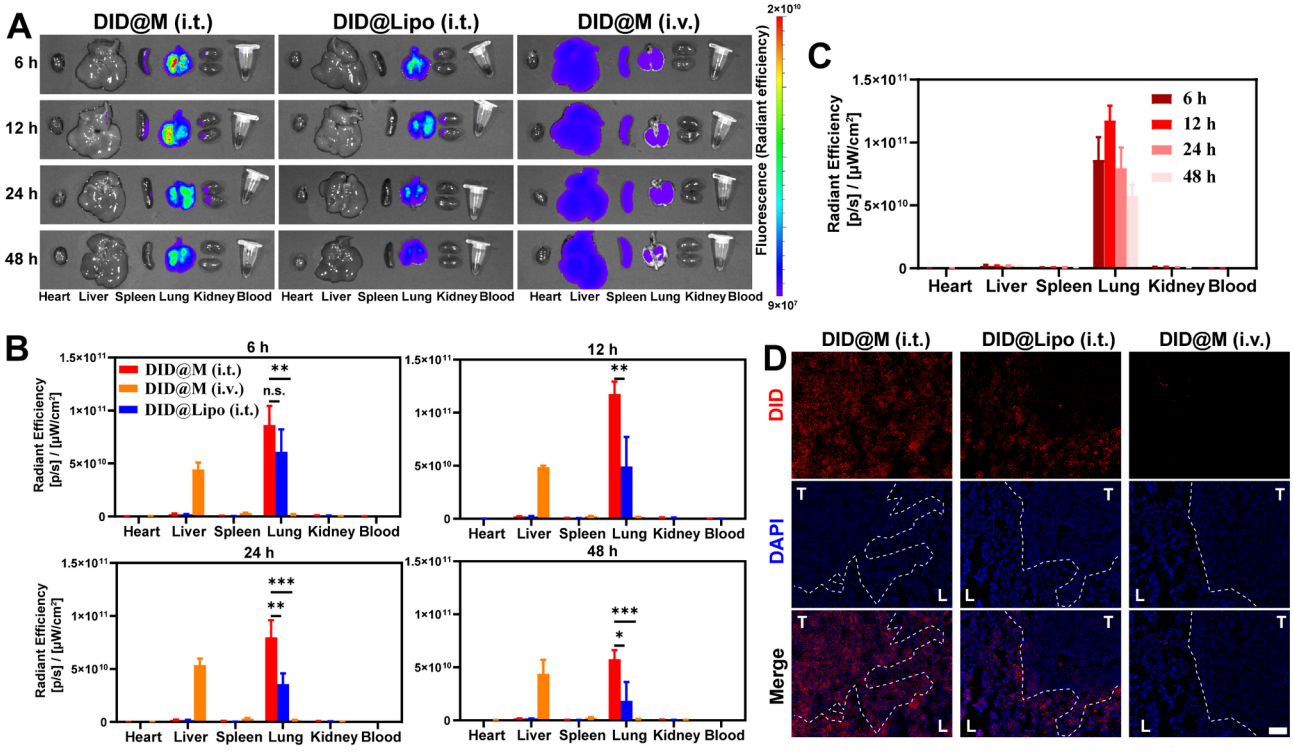

Fig. 6 The lung distribution of macrophage cell membrane-based nanovesicles. (**A**) Representative ex vivo images of DID fluorescence intensity in major organs dissected from mice at different time points after i.t. injected with DID@M, i.t. injected with DID@Lipo, or i.v. injected with DID@M. (**B**) The quantified results of ex vivo DID fluorescence intensity in major organs dissected from mice at 6 h, 12 h, 24 h, and 48 h ($n = 3$). (**C**) The quantified results of ex vivo DID fluorescence intensity in major organs dissected from mice at different time points after treated with DID@M (i.t.) ($n = 3$). (**D**) Localization of DID@M (i.t.), DID@Lipo (i.t.), or DID@M (i.v.) in orthotopic LLC lung cancer. T and L represent tumor region and lung region, respectively. The white dotted lines show tumor-lung border. Scale bar = 100 μm. *, **, and *** denote $p < 0.05$, $p < 0.01$, and $p < 0.001$, respectively

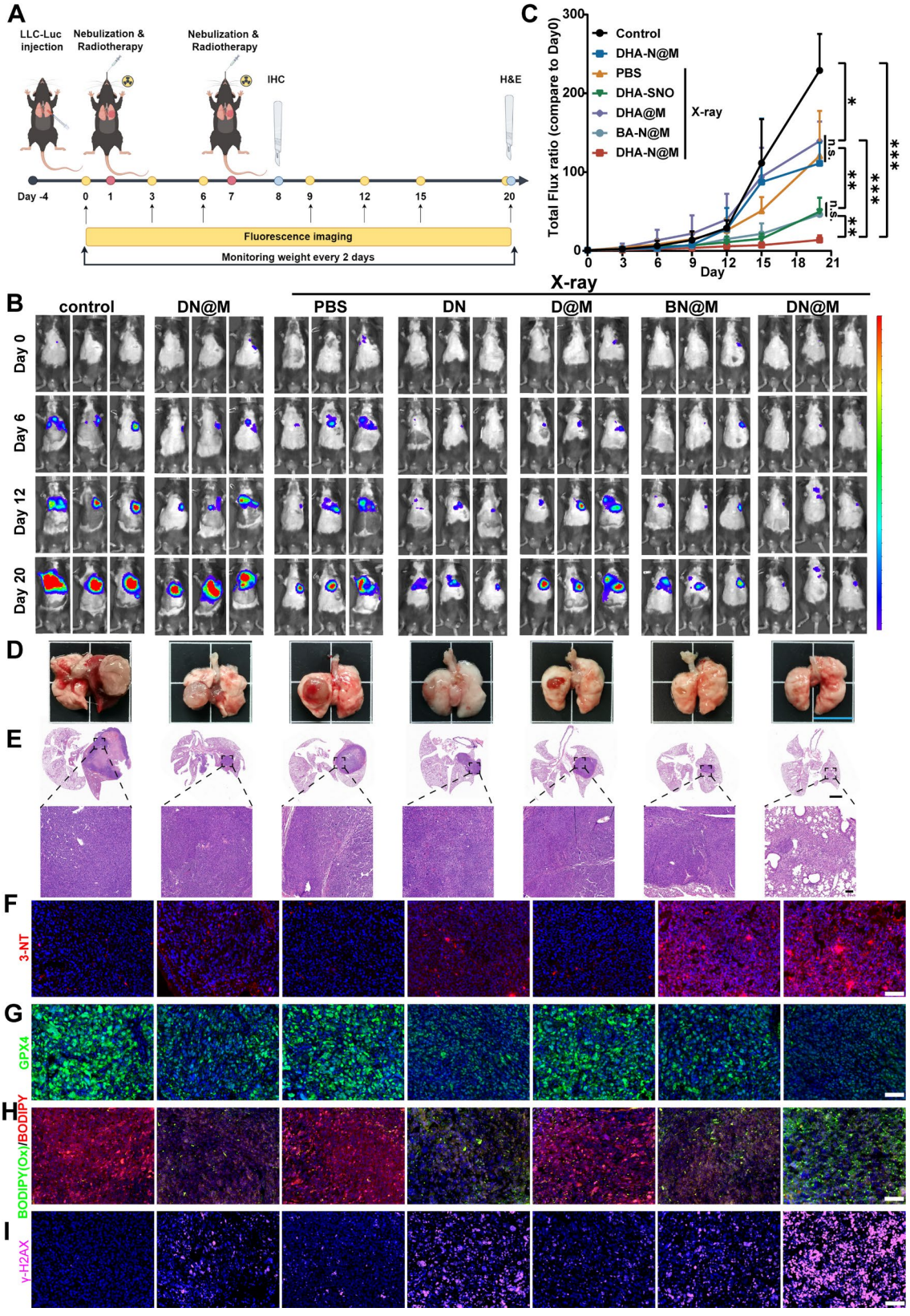

Fig. 7 (See legend on next page.)

(See figure on previous page.)

Fig. 7 In vivo combination therapy. (**A**) Schematic illustration of the treatment schedules in LLC-Luc orthotopic lung cancer model (Created by FigDraw). (**B**) Representative bioluminescence images of LLC-Luc orthoptic lung tumors in mice on day 0, 6, 12, and 20. (**C**) The tumor growth curves of LLC-Luc orthoptic lung cancer mice after different treatments monitored by the IVIS system ($n = 5$). (**D**) Representative images of lung tissues with LLC-Luc orthoptic lung tumor from each group in the end of experimentation; Scale bar = 1 cm. (**E**) Representative H&E staining images and enlarged view of lung tissues with LLC-Luc orthoptic lung tumor from each group in the end of experimentation; Scale bar = 1 mm for upper panel and 100 μm for lower panel. Immunofluorescence staining with (**F**) antibody against 3-NT (red) and (**G**) antibody against GPX4 (green). Scale bar = 50 μm. (**H**) Immunofluorescence analysis with C11-BODIPY$^{581/591}$ probe (BODIPY(Ox), LPO, green; BODIPY, LP, red). Scale bar = 50 μm. (**I**) Immunofluorescence staining with antibody against γ-H2AX (pink). Scale bar = 50 μm

other organs up to 48 h. More significantly, quantitative results from Fig. 6B showed that the average fluorescence intensity of inhaled DID@M in the lungs surpassed that of DID@Lipo, being 1.41-fold, 2.38-fold, 2.24-fold, and 3.12-fold higher at 6 h, 12 h, 24 h, and 48 h, respectively, and surpassed that of injected DID@M, being 48.30-fold, 70.32-fold, 44.09-fold, and 52.87-fold higher at 6 h, 12 h, 24 h, and 48 h, respectively. This result proved the superiority of inhaled RCM than inhaled liposome in distribution and retention in the lungs, benefiting from the biomimetic stealth effect of macrophage membrane and evasion of the mononuclear phagocyte system. The fluorescence intensity in the lungs post i.t. administration of DID@M peaked at 12 h, which was selected as the optimized time for X-ray irradiation, and decrease over time with a noticeable fluorescence signal at 48 h (Fig. 6C).

To further observe the tumor distribution of nanovesicles, the tumor-carrying lungs were harvested to make into sections 12 h post-administration. Tumor regions and lung regions can be differentiated according to cell nucleus density [51–53]. As displayed in Fig. 6D, the almost absence of fluorescence indicated the difficulty for i.v. injected DID@M to reach lungs. It could also be seen that i.t. administrated DID@Lipo was located in lungs and the border of tumor-lung, unable to penetrate deeply into tumor, whereas the i.t. administrated DID@M crossed the tumor-lung border and distributed uniformly in the interior of the tumor, attributed to the tumor tropism ability of macrophage [17, 27]. The above results collectively suggested that inhaled RCM provide a productive way to treat lung cancer.

In vivo antitumor effect

Inspired by the high accumulation of RCM at lung tumor after nebulization and the in vitro radiotherapeutic inhibitory activity, we further investigated the in vivo anticancer effect on C57BL/6 mice with LLC-Luc orthoptic lung tumors (Fig. 7A). As shown in Fig. 7B, 7C, and **S42**, the tumors in control groups grew at an incredibly rapid rate. After two cycles of inhalation-based radiotherapy, various degrees of tumor growth inhibition were observed in all treatment groups, among which DHA-N@M + X-ray treatment achieved the most effective tumor suppression (93.91%) with the weakest bioluminescence intensity. The antitumor effect was further confirmed by H&E staining. As displayed in Fig. 7D and E, there was a large solid tumor visible in the lung dissected from mouse without any treatment, nearly occupying the entire left lung, while the lung in DHA-N@M + X-ray group barely had detected tumor in macroscopic appearance, with the loosely arranged tumor cells in H&E image. This excellent antitumor effect of DHA-N@M was mainly attributed to the localized delivery *via* inhalation helping the nanoreactors accumulating in the lung and the tumor-tropism ability of macrophage cell membranes directing the nanoreactors at the tumor site. In the meantime, the DHA-N@M accumulated at the tumor sites could disintegrate to release NO and DHA under reductive TME, and subsequently triggered ferroptosis upon X-ray irradiation *via* $ONOO^-$ generation, GSH/GPX4 depletion, DHA oxidation, and LPO production.

To explore the anti-neoplastic mechanism, tumor-bearing lungs were harvested within 24 h after the completion of the second round of treatment and then immunofluorescence stained with 3-NT antibody, GPX4 antibody, LPO probe, and γ-H2AX antibody, respectively. In line with the cytological study, the DHA-N@M + X-ray group exhibited the highest level of 3-NT, confirming the formation of $ONOO^-$ and the high nitrosative stress in tumor tissue (Fig. 7F and **S43**). After DHA-N@M + X-ray therapy, the significant decrease in green fluorescence representing GPX4 indicated the complete collapse of the tumor's reductive defense mechanism (Fig. 7G and **S44**), while the substantial increase in the ratio of green/red fluorescence of the C11-BODIPY$^{581/591}$ probe suggested the accumulation of LPO (Fig. 7H and **S45**). Together, these two observations unveiled the occurrence of ferroptosis in the tumor tissue. Moreover, the most severe DNA damage was observed in DHA-N@M + X-ray group (Fig. 7I and **S46**). These data collectively supported that DHA-N@M inhalation combined with radiotherapy would be a promising treatment approach against lung cancer.

Finally, the in vivo biosafety of DHA-N@M was preliminarily evaluated. As shown in **Fig. S47**, the body weight varied in a small range (less than ± 10%). In addition, no evident histopathological changes were observed in H&E staining of major organs and the tracheas maintained intact (**Fig. S48**). These results indicated the satisfactory safety of DHA-N@M for in vivo application.

Discussion

Inhalation therapy, primarily evolved for the clinical treatment of asthma and chronic obstructive pulmonary disorder, also shows promise for lung cancer treatment. Although systemic administration routes (e.g., intravenous or oral), have served as the cornerstone of treatment of lung cancer, they face critical bottlenecks, such as blood-air barrier, extremely low drug accumulation in tumor site, and pronounced systemic toxicity [54]. In contrast, inhalation approach offers non-invasiveness, rapid onset of pharmacologic action, minimal off-target effects, and enhanced pulmonary drug accumulation. Recent studies have validated the feasibility of novel nanoparticles for lung cancer treatment, including liposome [55], exosome [47, 48], and nanoemulsion [56]. For the first time, we conducted a proof-of-concept for the design and preclinical use of cell membrane-based nanovesicles in inhalation therapy for lung cancer. Our findings demonstrated that cell membrane-based nanovesicles could withstand the shear forces and high pressure generated during nebulization (**Fig. S38**). In addition, pulmonary delivery of cell membrane-based nanovesicles mainly targeted to the lungs and tumors, while most intravenous nanovesicles accumulated in the livers (Fig. 6A ~ 6C).

Although inhalation therapy exhibits reduced systemic toxicity, the potential pulmonary toxicity needs to be considered due to the inevitable exposure of healthy lung tissue to inhaled drug which is distributed equally among the lung parenchyma [57]. To address this challenge, we rationally designed DHA-N@M nanoreactors with tumor-tropism capacity and GSH-responsive NO release ability that can reduce nonspecific toxicity in normal lung tissue. In Fig. 7E, representative H&E staining of lung from DHA-N@M + X-ray group showed that only a small residual tumor located in the left lung, while the surrounding parenchyma and contralateral right lung maintained normal tissue architecture. No significant differences in body weight or in H&E staining of major organs were observed between the DHA-N@M + X-ray group and the control group, indicating no systemic toxicity during the treatment period (**Fig. S47** and **Fig. S48**). It should be noted, due to the gaseous and short-lived nature of NO and $ONOO^-$, the likelihood of delayed and accumulated toxicity after the completion of treatment is minimal [58, 59]. The combined evidence suggested minimal pulmonary toxicity and robust safety characteristics of DHA-N@M nanoreactors.

Numerous studies have substantiated that radiotherapy can induce lipid peroxidation and ferroptosis represents a critical mechanism underlying radiation-mediated anticancer effects, confirming the rationality of the therapeutic strategy combing radiotherapy with ferroptosis-inducing nanoparticles [60, 61]. Mechanistically, the synergy between radiotherapy and ferroptosis hinges on metabolic reprogramming and amplified oxidative stress cascades. The ionizing radiation generates ROS, causing oxidative stress, that not only directly damage tumor cells but also drive PUFA-PL peroxidation, thereby triggering ferroptosis execution. Capitalizing on this insight, we designed DHA-N@M nanoreactors not only to intensify oxidative stress through GSH depletion and NO/$ONOO^-$ generation but also to modulate lipid metabolism *via* PUFA supplement, creating a coordinated therapeutic axis that potently enhances ferroptosis and tumor suppression. In vivo, DHA-N@M + X-ray significantly suppressed tumor growth (93.91% inhibition), outperforming X-ray monotherapy (22.9% inhibition, $p < 0.001$), highlighting the dominant contribution of oxidative stress amplification, lipid metabolic intervention, and consequent ferroptosis potentiation (Fig. 7B ~ 7E). Although a serials of control groups were set, including DHA-SNO + X-ray, DHA@M + X-ray, and BA-N@M + X-ray, the inherent dynamic crosstalk and reciprocally regulation between oxidative stress, lipid metabolism [62], and ferroptosis pathways, makes it challenging to precisely quantify the individual contributions of specific mechanisms (NO/$ONOO^-$ generation, GSH depletion, and lipid metabolic interference) to the overall therapeutic outcome.

Several important questions remain to be addressed in subsequent studies. First, given that the lung represents a common metastatic site for breast cancer and melanoma [63, 64], the inhalation approach offers unique advantage by enabling nanovesicle delivery to multiple pulmonary lesions/lobes at the same time [65]. Therefore, establishing pulmonary metastasis models to evaluate the radiotherapeutic efficacy of inhaled DHA-N@M would be highly valuable. Second, multiple type of cell membranes has been extensively studied in biomimetic nanotechnology [66], thus, systematic screening is required to identify the optimal membrane-based delivery system for inhaled lung cancer therapy. Third, considering that ferroptosis, radiotherapy, and $ONOO^-$ all have potential to modulate the tumor immune microenvironment [37, 65], combination DHA-N@M + X-ray treatment with immunotherapy may yield synergistic therapeutic benefits. Finally, comprehensive long-term safety assessments remain essential to fully evaluate the clinical potential of this therapeutic strategy.

Conclusion

In this study, we rationally synthesized a functionalized PUFA (DHA-SNO) with GSH-responsive NO release capability and firstly designed a macrophage cell-inspired inhalable nanoreactor of DHA-N@M to achieve enhanced lung tumor accumulation and excellent ferroptosis-radiotherapy. This inhalable biomimetic

nanoreactor exhibit a spectrum of the following application superiorities. (1) The local administration route *via* inhalation and the macrophage cell membrane-based nanovesicle with tumor-tropism ability jointly facilitate satisfactory accumulation of DHA-N@M at lung tumor to pursue maximized therapeutic efficacy. (2) In terms of antitumor mechanism, DHA-N@M nanoreactor couples two cascade reactions under X-ray irradiation, including SNO-participated reaction for depleting GSH and generating NO, and ROS-participated reactions for forming highly cytotoxic $ONOO^-$ and oxidizing PUFA. Ultimately, in vitro potent cytotoxicity andin vivo satisfactory tumor suppression effect were achieved by joint ferroptosis and radiotherapy. Overall, the unique inhalable DHA-N@M led to new insights into enhanced ferroptosis-radiotherapy against lung cancer.

Supplementary Information

The online version contains supplementary material available at https://doi.org/10.1186/s12951-025-03409-8.

Supplementary Material 1

Acknowledgements
This work was supported by the National Natural Science Foundation of China (82473856) and the National Key R&D Program of the Ministry of Science and Technology (2022YFC2304303). We thank Home for Researchers (www.home-for-researchers.com) for the scheme drawing. We thank Jialin Duan and Guangyi Li in the National Center for Protein Science Shanghai for their technical assistance on Cryo-TEM. We would like to thank Scientific Compass (www.shiyanjia.com) for support with the Bio-TEM and Shanghai Bioprofile Technology Co., Ltd for the target lipidomics analysis. We thank the National Center for Protein Science Shanghai for providing RS-2000 irradiator.

Author contributions
Conceptualization: YC, XS, ZZ; In vitro studies: YC, XH, EL, KL; In vivo studies: YC, XH, RH, XY; Statistical analysis: EL. KL, YX; Funding acquisition: XS; Supervision: XS, ZW, YM, MZ; Writing– original draft: YC, XH; Writing– review & editing: XS, ZW, YM, MZ.

Data availability
No datasets were generated or analysed during the current study.

Declarations

Ethics approval and consent to participate
All the animal experimental procedures were in accordance with the guidelines for the Care and Use of Laboratory Animals of Fudan University and approved by the Institutional Animal Care and Use Committee of the School of Pharmacy, Fudan University.

Consent for publication
All authors agree to be published.

Competing interests
The authors declare no competing interests.

Electronic supporting materials
Supplementary data associated with this article can be found in the online version.

Received: 26 January 2025 / Accepted: 19 April 2025
Published online: 08 May 2025

References

1. Bray F, Laversanne M, Sung H, et al. Global cancer statistics 2022: GLOBOCAN estimates of incidence and mortality worldwide for 36 cancers in 185 countries. CA Cancer J Clin May-Jun. 2024;74(3):229–63.
2. Timmerman R, Paulus R, Galvin J, et al. Stereotactic body radiation therapy for inoperable early stage lung cancer. JAMA Mar. 2010;17(11):1070–6.
3. Bradley JD, Paulus R, Komaki R, et al. Standard-dose versus high-dose conformal radiotherapy with concurrent and consolidation carboplatin plus Paclitaxel with or without cetuximab for patients with stage IIIA or IIIB non-small-cell lung cancer (RTOG 0617): a randomised, two-by-two factorial phase 3 study. Lancet Oncol Feb. 2015;16(2):187–99.
4. Zhang Y, Sha R, Zhang L, et al. Harnessing copper-palladium alloy tetrapod nanoparticle-induced pro-survival autophagy for optimized photothermal therapy of drug-resistant cancer. Nat Commun Oct. 2018;12(1):4236.
5. Hanahan D. Hallmarks of cancer: new dimensions. Cancer Discov Jan. 2022;12(1):31–46.
6. Dixon SJ, Lemberg KM, Lamprecht MR, et al. Ferroptosis: an iron-dependent form of nonapoptotic cell death. Cell May. 2012;25(5):1060–72.
7. Lei G, Zhang Y, Koppula P, et al. The role of ferroptosis in ionizing radiation-induced cell death and tumor suppression. Cell Res Feb. 2020;30(2):146–62.
8. Mura S, Nicolas J, Couvreur P. Stimuli-responsive nanocarriers for drug delivery. Nat Mater Nov. 2013;12(11):991–1003.
9. Diehn M, Cho RW, Lobo NA, et al. Association of reactive oxygen species levels and radioresistance in cancer stem cells. Nat Apr. 2009;9(7239):780–3.
10. Xiao W, Zhao L, Sun Y, Yang X, Fu Q. Stimuli-Responsive nanoradiosensitizers for enhanced Cancer radiotherapy. Small Methods Jan. 2024;8(1):2301131.
11. Yang YQ, Huang ZJ, Li LL. Advanced nitric oxide donors: chemical structure of NO drugs, NO nanomedicines and biomedical applications. Nanoscale Jan. 2021;14(2):444–59.
12. Huang ZJ, Fu JJ, Zhang YH. Nitric oxide Donor-Based Cancer therapy: advances and prospects. J Med Chem Sep. 2017;28(18):7617–35.
13. Shi M, Zhang J, Wang Y, et al. Tumor-specific nitric oxide generator to amplify peroxynitrite based on highly penetrable nanoparticles for metastasis Inhibition and enhanced cancer therapy. Biomaterials Apr. 2022;283:121448.
14. Sung YC, Jin PR, Chu LA, et al. Delivery of nitric oxide with a nanocarrier promotes tumour vessel normalization and potentiates anti-cancer therapies. Nat Nanotechnol Dec. 2019;14(12):1160–9.
15. Anselmo AC, Gokarn Y, Mitragotri S. Non-invasive delivery strategies for biologics. Nat Rev Drug Discovery Jan. 2019;18(1):19–40.
16. Lokugamage MP, Vanover D, Beyersdorf J, et al. Optimization of lipid nanoparticles for the delivery of nebulized therapeutic mRNA to the lungs. Nat Biomed Eng Sep. 2021;5(9):1059–68.
17. Zhao HJ, Li L, Zhang JL, et al. C-C chemokine ligand 2 (CCL2) recruits Macrophage-Membrane-Camouflaged Hollow bismuth Selenide nanoparticles to facilitate photothermal sensitivity and inhibit lung metastasis of breast Cancer. ACS Appl Mater Interfaces Sep. 2018;19(37):31124–35.
18. Kong DH, Kim YK, Kim MR, Jang JH, Lee S. Emerging roles of vascular cell adhesion Molecule-1 (VCAM-1) in immunological disorders and Cancer. Int J Mol Sci Apr. 2018;19(4):1057.
19. Schmall A, Al-Tamari HM, Herold S, et al. Macrophage and Cancer cell Cross-talk via CCR2 and CX3CR1 is a fundamental mechanism driving lung Cancer. Am J Respir Crit Care Med Feb. 2015;15(4):437–47.
20. Nagy-Major K, Sänger J, Kulkarni HR, et al. Chemokine receptor signaling as a new tool to improve lung cancer diagnostics and therapy. Cancer Res Jul. 2017;77:944.
21. He WX, Zhang XY, Gong X, et al. Drug-Free biomimetic oxygen supply nanovehicle promotes Ischemia-Reperfusion therapy in stroke. Adv Funct Mater May. 2023;33(21):2212919.
22. Fang RNH, Hu CMJ, Chen KNH, et al. Lipid-insertion enables targeting functionalization of erythrocyte membrane-cloaked nanoparticles. Nanoscale. 2013;5(19):8884–8.
23. Chai ZL, Ran DN, Lu LW, et al. Ligand-Modified cell membrane enables the targeted delivery of drug nanocrystals to glioma. ACS Nano May. 2019;13(5):5591–601.
24. Yu WW, Wang Z, Yu XF, et al. Kir2.1-mediated membrane potential promotes nutrient acquisition and inflammation through regulation of nutrient transporters. Nat Commun Jun. 2022;21(1):3544.
25. Rousseau BJG, Soudackov AV, Tuttle RR, Reynolds MM, Finke RG, Hammes-Schiffer S. Computational insights into the mechanism of nitric oxide generation from S-Nitrosoglutathione catalyzed by a copper Metal-Organic framework. J Am Chem Soc May. 2023;10(18):10285–94.

26. Zhou Y, Tan JY, Dai YP, Yu YM, Zhang Q, Meyerhoff ME. Synthesis and nitric oxide releasing properties of novel fluoro S-nitrosothiols. Chem Commun Jan. 2019;11(3):401–4.
27. Cao HQ, Dan ZL, He XY, et al. Liposomes coated with isolated macrophage membrane can target lung metastasis of breast cancer. ACS Nano Aug. 2016;10(8):7738–48.
28. Zhang D, Lin ZG, Zheng YS, et al. Ultrasound-Driven biomimetic nanosystem suppresses tumor growth and metastasis through sonodynamic therapy, CO therapy, and indoleamine 2,3-Dioxygenase Inhibition. ACS Nano Jul. 2020;28(7):8985–99.
29. Chou TC. Theoretical basis, experimental design, and computerized simulation of synergism and antagonism in drug combination studies. Pharmacol Rev Sep. 2006;58(3):621–81.
30. Kim H, Xue X. Detection of total reactive oxygen species in adherent cells by 2,7-Dichlorodihydrofluorescein diacetate staining. J Vis Exp Jun 2020(160):60682.
31. Taskiran AS, Ergul M. The modulator action of thiamine against pentylenetetrazole-induced seizures, apoptosis, nitric oxide, and oxidative stress in rats and SH-SY5Y neuronal cell line. Chem Biol Interact May. 2021;1:340:109447.
32. Zhang KZ, Kaufman RJ. From endoplasmic-reticulum stress to the inflammatory response. Nat Jul. 2008;24(7203):455–62.
33. Liu SK, Li WT, Ding H, et al. Biomineralized RuO_2 nanozyme with Multi-Enzyme activity for Ultrasound-Triggered Peroxynitrite-Boosted ferroptosis. Small Nov. 2023;8(45):2303057.
34. Huang L, Zhu JY, Xiong W, et al. Tumor-Generated reactive oxygen species storm for High-Performance ferroptosis therapy. ACS Nano Jun. 2023;7(12):11492–506.
35. Liu NH, Zhu JJ, Zhu WJ, et al. X-ray-Induced release of nitric oxide from Hafnium-Based nanoradiosensitizers for enhanced Radio-Immunotherapy. Adv Mater Jul. 2023;35(29):2302220.
36. Doll S, Proneth B, Tyurina YY, et al. ACSL4 dictates ferroptosis sensitivity by shaping cellular lipid composition. Nat Chem Biol Jan. 2017;13(1):91–8.
37. Yang LJ, Wang DY, Jia HX, et al. Tumor-Specific peroxynitrite overproduction disrupts metabolic homeostasis for sensitizing melanoma immunotherapy. Adv Mater Jul. 2023;35(29):2301455.
38. Liu SK, Li WT, Chen HX, et al. On-Demand generation of peroxynitrite from an integrated Two-Dimensional system for enhanced tumor therapy. ACS Nano Jun. 2022;28(6):8939–53.
39. Chen PH, Tseng WHS, Chi JT. The intersection of DNA damage response and Ferroptosis-A rationale for combination therapeutics. Biology-Basel Aug. 2020;9(8):187.
40. Tang DL, Chen X, Kang R, Kroemer G. Ferroptosis: molecular mechanisms and health implications. Cell Res Feb. 2021;31(2):107–25.
41. Song EA, Kim H. Docosahexaenoic acid induces oxidative DNA damage and apoptosis, and enhances the chemosensitivity of Cancer cells. Int J Mol Sci Aug. 2016;17(8):1257.
42. Yang WS, Kim KJ, Gaschler MM, Patel M, Shchepinov MS, Stockwell BR. Peroxidation of polyunsaturated fatty acids by lipoxygenases drives ferroptosis. Proc Natl Acad Sci U S Aug. 2016;23(34):4966–75.
43. Dierge E, Debock E, Guilbaud C, et al. Peroxidation of n-3 and n-6 polyunsaturated fatty acids in the acidic tumor environment leads to ferroptosis-mediated anticancer effects. Cell Metab Aug. 2021;3(8):1701–15.
44. Kagan VE, Mao GW, Qu F, et al. Oxidized arachidonic and adrenic PEs navigate cells to ferroptosis. Nat Chem Biol Jan. 2017;13(1):81–90.
45. Zhang Y, Tan H, Daniels JD, et al. Imidazole ketone Erastin induces ferroptosis and slows tumor growth in a mouse lymphoma model. Cell Chem Biol May. 2019;16(5):623–33.
46. Bi GS, Liang JQ, Shan GY, et al. Retinol saturase mediates retinoid metabolism to impair a ferroptosis defense system in Cancer cells. Cancer Res Jul. 2023;15(14):2387–404.
47. Popowski KD, Lopez de Juan Abad B, George A, et al. Inhalable exosomes outperform liposomes as mRNA and protein drug carriers to the lung. Extracell Vesicle Dec. 2022;1:100002.
48. Liu MR, Hu SQ, Yan N, Popowski KD, Cheng K. Inhalable extracellular vesicle delivery of IL-12 mRNA to treat lung cancer and promote systemic immunity. Nat Nanotechnol Jan. 2024;11:19:565–75.
49. Xu Y, Liu H, Song L. Novel drug delivery systems targeting oxidative stress in chronic obstructive pulmonary disease: a review. J Nanobiotechnol Oct. 2020;19(1):145.
50. Stillman ZS, Decker GE, Dworzak MR, Bloch ED, Fromen CA. Aluminum-based metal-organic framework nanoparticles as pulmonary vaccine adjuvants. J Nanobiotechnol Feb. 2023;3(1):39.
51. Ma SQ, Cong ZQ, Wei JX, et al. Pulmonary delivery of size-transformable nanoparticles improves tumor accumulation and penetration for chemo-sonodynamic combination therapy. J Controlled Release Oct. 2022;350:132–45.
52. Situ B, He BR, Chen X, et al. Fluorescent sensing of nucleus density assists in identifying tumor cells using an AIE luminogen. Chem Eng J Apr. 2021;15:410:128183.
53. Hernandez-Verdun D. The nucleolus: a model for the organization of nuclear functions. Histochem Cell Biol Aug. 2006;126(2):135–48.
54. Gandhi S, Roy I. Lipid-Based inhalable Micro- and nanocarriers of active agents for treating Non-Small-Cell lung Cancer. Pharm May 10 2023;15(5).
55. Fu F, Wang W, Wu L, et al. Inhalable biomineralized liposomes for Cyclic Ca(2+)-Burst-Centered Endoplasmic reticulum stress enhanced lung Cancer ferroptosis therapy. ACS Nano Mar. 2023;28(6):5486–502.
56. Yang J, Li Y, Sun J, et al. An Osimertinib-Perfluorocarbon nanoemulsion with excellent targeted therapeutic efficacy in Non-small cell lung cancer: achieving intratracheal and intravenous administration. ACS Nano Aug. 2022;23(8):12590–605.
57. Lee WH, Loo CY, Ghadiri M, Leong CR, Young PM, Traini D. The potential to treat lung cancer via inhalation of repurposed drugs. Adv Drug Deliv Rev Aug. 2018;133:107–30.
58. Wang Z, Jin A, Yang Z, Huang W. Advanced nitric oxide generating nanomedicine for therapeutic applications. ACS Nano May. 2023;23(10):8935–65.
59. Lee J, Hlaing SP, Hasan N, et al. Tumor-Penetrable nitric Oxide-Releasing nanoparticles potentiate local antimelanoma therapy. ACS Appl Mater Interfaces Jul. 2021;7(26):30383–96.
60. Liu X, Cao Z, Wang W, et al. Engineered extracellular Vesicle-Delivered CRISPR/Cas9 for radiotherapy sensitization of glioblastoma. ACS Nano Sep. 2023;12(17):16432–47.
61. Cao Z, Liu X, Zhang W, et al. Biomimetic macrophage Membrane-Camouflaged nanoparticles induce ferroptosis by promoting mitochondrial damage in glioblastoma. ACS Nano Dec. 2023;12(23):23746–60.
62. Mou Y, Wang J, Wu J, et al. Ferroptosis, a new form of cell death: opportunities and challenges in cancer. J Hematol Oncol Mar. 2019;29(1):34.
63. Xiao W, Zheng S, Liu P, et al. Risk factors and survival outcomes in patients with breast cancer and lung metastasis: a population-based study. Cancer Med Mar. 2018;7(3):922–30.
64. Tas F. Metastatic behavior in melanoma: timing, pattern, survival, and influencing factors. J Oncol. 2012;2012:647684.
65. Liu Y, Crowe WN, Wang L, et al. An inhalable nanoparticulate STING agonist synergizes with radiotherapy to confer long-term control of lung metastases. Nat Commun Nov. 2019;8(1):5108.
66. Fang RH, Gao W, Zhang L. Targeting drugs to tumours using cell membrane-coated nanoparticles. Nat Rev Clin Oncol Jan. 2023;20(1):33–48.

Publisher's note